Master Thesis

Faculty of Engineering Technology (CTW)

Output-only Modal-based Structural Health Monitoring in composite beams

G.E. Teunis

Document Number:
CTW.15/TM-5755

Date:
July 29, 2015

Examination Committee:
prof. dr. ir. T. Tinga
dr. ir. R. Loendersloot
dr. ir. L. Warnet

UNIVERSITY OF TWENTE.

MASTER THESIS

Output-only Modal-based Structural Health Monitoring in composite beams

Student

Name Ruben Teunis

Student number s1112392

University

Institution University of Twente

Faculty Engineering Technology

Master Mechanical Engineering

Chair Dynamics Based Maintenance

Supervision Prof.dr.ir. T. Tinga & dr.ir. R. Loendersloot

City & Country Enschede, The Netherlands

Date July 29, 2015

UNIVERSITY OF TWENTE.

Preface

This report is the result of my master thesis performed at the Dynamics Based Maintenance chair for the Masters Degree in Mechanical Engineering at the University of Twente. For this thesis, I performed experimental work on an experimental setup with the aim to implement structural health monitoring techniques while only using operational vibrations.

I would like to thank some people for helping me during this assignment. First of all, I would like to thank Richard. Despite the fact that the process was not always easy, you always helped me with your encouragement and endless corrections on the preliminary reports. I really appreciate everything you have done for me. Next, I thank Tiedo for making this thesis possible at the chair of Dynamics Based Maintenance. Thanks for your critical view and questions during our meetings.

Finally, I would like to thank my family, friends and fellow students for their moral support the last couple of months. Especially, I like to thank my parents for their endless financial and moral support and Andrea, without you I would never have survived the past two years.

Summary

Composite materials are frequently used in airplanes and aviation applications like helicopters. Damages in composite materials are in most cases complex and hard to detect. To obtain the real condition of the blades structural health monitoring technology can be applied. In this way, the composite materials can be used more safely and effectively.

The research question is stated as follows:

- *To what extend can damage in a composite beam structure, subjected to rotor blade system boundary conditions, be detected with modal-based techniques while only using output data ?*

The following sub questions are formulated:

- *Can a properly working test setup with reduced complexity be obtained ?*
- *Are operational modal analysis techniques suitable to detect damage in the test setup ?*
- *Is there a distinction in the detectability of different composite damage scenarios ?*

To be able to answer these questions a less complex and more robust redesign of an existing experimental setup is proposed. Subsequently, a composite blade is introduced. The obtained setup is able to show a flapping motion with different possible boundary conditions. The classical lamination theory is applied to estimate the blade mechanical properties. Also, the mode shapes and corresponding natural frequencies are analytically calculated to show the extreme clamped and hinged behavior of the setup.

In this thesis the modal curvature damage index and modal strain energy damage index are applied on a composite blade. Both methods use mode shapes as input parameters. The mode shapes can be extracted from the measurement data with either the experimental modal analysis or operational modal analysis technique. These methods differ from each other, because the first one uses both input and output data of the system and the second method only uses output data. The aim in this research is to use the output only method, but the experimental method is mostly used in practice and therefore the results will be compared.

The modal assurance criterion gives an indication of the correspondence of two mode shapes. The criterion is used to asses the repeatability of both modal methods and the performance of the operational method. It is concluded that the measurements are highly

repeatable and the operational method shows satisfying results. two boundary condition cases can be recognized which both show approximately clamped beam behavior. The amount of noise is however larger in one of the cases, therefore both will be used to apply damage on.

Point masses are added to simulate damage because this makes it possible to assess a lot more damage scenarios with only one blade. Also, damage scenarios can be repeated with this approach. For the single damage scenarios it can be concluded that it is possible to set a threshold peak value to detect damage. It is also possible to localize the damage within a certain distance and determine accumulating severity. Furthermore, it can be observed that the noise level is higher at one of the boundary condition cases and the performance of this case is also less. In the multiple damage scenarios it is more difficult to determine the damage locations with confidence. With equal damages it is only possible to identify the damage location for one boundary condition case. The higher noise level makes that the peaks are not high enough in the other case. For unequal damage severity, only one out of four considered scenarios showed good results.

It is concluded that output only modal-based techniques are successfully implemented on a composite blade experimental setup. The behavior of the setup is a step towards an actual rotor blade system. It can be concluded that a robust SHM system can be developed while the damages are concentrated on one location. It turns out to be very difficult to draw any conclusions on the health of the blade when multiple damages are present.

Samenvatting

Composiet materialen worden veel gebruikt in vliegtuigen en andere luchtvaart toepassingen, zoals helikopters. Het schadegedrag van composiet materialen is vaak complex en bovendien is het moeilijk om de schades te detecteren. De actuele conditie van helikopter bladen kan verkregen worden door structural health monitoring technieken toe te passen. Met deze technieken wordt het mogelijk om de composiet materialen veiliger en effectiever te gebruiken.

De onderzoeksvraag is als volgt geformuleerd:

- *In hoeverre kan schade in een composiet blad structuur, onderhevig aan rotor blade systeem randcondities, gedetecteerd worden met modaal analyse technieken wanneer alleen uitgangsdata gebruikt wordt ?*

De volgende subvragen zijn geformuleerd:

- *Kan een goed werkende experimentele opstelling met verminderde complexiteit verkregen worden ?*
- *Zijn operationele modaal analyse technieken geschikt om schade te detecteren in de experimentele opstelling ?*
- *Is er verschil in de detecteerbaarheid van verschillende composiet schade scenario's ?*

Om deze vragen te kunnen beantwoorden is een minder complex, maar robuuster herontwerp van een bestaande experimentele opstelling voorgesteld. Vervolgens is ook een composiet blad geïntroduceerd. De verkregen setup is in staat om een flappende beweging te laten zien met verschillende randvoorwaardes. De klassieke laminatie theorie is toegepast om de mechanische eigenschappen van het blad te benaderen. Daarnaast zijn de eigenmodes en eigenfrequenties analytisch bepaald om de extreme ingeklemde en scharnierende eigenschappen van de setup te laten zien.

In deze scriptie zullen de modal curvature schade index en de modal strain energy schade index toegepast worden op een composiet blad. Beide methodes maken gebruik van eigenmodes als invoer parameter. De eigenmodes kunnen uit de meet data gehaald worden met experimentele en operationele modaal analyse. Deze methodes verschillen in het feit dat de eerste ingangs- en uitgangsdata gebruikt en de tweede alleen uitgangsdata van de opstelling. Het doel is om de operationele methode te gebruiken. De experimentele methode is echter het meeste gebruikt in de praktijk en daarom zullen de beide methoden

vergeleken worden.

Het modal assurance criterion geeft een indicatie van de overeenkomst van twee eigenmodes. het criteria is gebruikt om de herhaalbaarheid van beide methodes en de prestaties van de operationele methode te beoordelen. Er is geconcludeerd dat de metingen goed repeteerbaar zijn en dat de operationele methode goede resultaten geeft. Twee randvoorwaarde gevallen kunnen herkend worden die beide bij benadering ingeklemd gedrag vertonen. De hoeveelheid ruis is echter groter in een van de gevallen. Daarom zullen beide gevallen gebruikt worden om schade te bepalen.

Punt massa's zijn gebruikt om schade te simuleren omdat dit het mogmaakt om veel meer schade scenario's te beoordelen met hetzelfde blad. Ook kunnen de schade scenario's herhaald worden op deze manier. Er wordt onderscheid gemaakt tussen gevallen met één of twee toegevoegde massa's. Bij de één toegevoegde massa scenario's kan geconcludeerd worden dat het mogelijk is om een piek drempelwaarde te stellen om schade te detecteren. Ook is het mogelijk om schade te lokaliseren in een klein oppervlak en te bepalen dat een schade groter wordt. Verder kan opgemerkt worden dat het ruisniveau bij 1 van de randcondities hoger ligt dan bij de andere. De prestaties van dit geval zijn ook minder. In de meerdere schade scenario's is het moeilijker om de schade locaties met zekerheid te bepalen. Bij gelijke schade grote is het alleen mogelijk om de schade locatie te bepalen voor één randvoorwaarde geval. Het hoge ruisniveau zorgt ervoor dat de pieken niet hoog genoeg zijn in het andere geval. Voor ongelijke schades laat maar één van de vier scenario's goede resultaten zien.

Het is geconcludeerd in deze studie dat operationele modaal analyse technieken succesvol toegepast zijn op een composiet blad in een experimentele setup. Het gedrag van de setup is een stap in de richting van daadwerkelijk rotor blad systeem. Het kan geconcludeerd worden dat een robuust structural health monitoring systeem ontwikkeld kan worden als de schade geconcentreerd is op één locatie. Het blijkt erg moeilijk om een conclusie te trekken over de conditie van het blad als meerdere schades aanwezig zijn.

Nomenclature

List of Abbreviations

DBM	Dynamics Based Maintenance
CPSD	Cross Power Spectral Density.
DOF	Degree of Freedom
EMA	Engineering Modal Analysis
FDD	Frequency Domain Decomposition.
FRF	Frequency Response Function
MAC	Modal Assurance Criterion.
MC-DI	Modal Curvature damage index
MSE-DI	Modal Strain Energy damage index
OMA	Operational Modal Analysis
PPS	Poly-Phenylene Sulphide
PSD	Power Spectral Density.
SHM	Structural Health Monitoring
TPRC	Thermoplastic Composite Research Center
VCM	Voice Coil Motor

List of Symbols

A	Area.
$[a]$	Inverse laminate extensional stiffness matrix.
$[A]$	Laminate extensional stiffness matrix.
$[C]$	Stiffness matrix.
$[C^*]$	Transformed stiffness matrix.
E_1	Layer longitudinal elasticity modulus.
E_2	Layer transverse elasticity modulus.
E_{1f}	Carbon fiber elasticity modulus in fiber direction.
E_{2f}	Carbon fiber elasticity modulus transverse to the fibers.
E_m	PPS matrix elasticity modulus.
E_x	Blade elasticity modulus in length direction.
E_y	Blade elasticity modulus in width direction.

$f(x,t)$	Distributed bending load as function of place and time.
$f(t)$	Excitation measurement data in time domain.
$F(\omega)$	Excitation measurement data in frequency domain.
F	Fraction of energy.
G_{12}	Layer shear modulus.
G_{12f}	Carbon fibers in-plane shear modulus.
G_m	PPS Matrix shear modulus.
G_{xy}	Blade in-plane shear modulus.
$G_{ff}(\omega)$	Input power spectral density.
$G_{uf}(\omega)$	Input-output power spectral density.
h	Laminate thickness.
$H(\omega)$	Frequency response function in the frequency domain.
I	Area moment of inertia.
L	Length of the composite blade.
m	Mass of the blade.
$M(x)$	Applied bending moment.
N	Number of composite layers.
N	Number of elements.
$[R]$	Reuter matrix.
t	Thickness of the composite blade.
$[T]$	Transformation matix.
u	Displacement in length direction.
$u(t)$	Response measurement data in time domain.
U	Strain energy.
$U(\omega)$	Response measurement data in frequency domain.
v_f	Fiber volume fraction.
v_m	Matrix volume fraction.
V	Volume.
w	Displacement perpendicular on the blade.
w	Width of the composite blade.
w_r	Vibration amplitude at every time step.
x	Blade length coordinate.
y	Blade width coordinate.
$y(x,t)$	Transverse vibration of the blade.
z	Blade thickness coordinate.
z_k	Blade thickness position.
Z_j	Normalized modal strain energy damage index.
β	constant.
β_j	Modal strain energy damage index.
γ	Engineering shear component.
Δ	Modal curvature damage index.
ε	Strain tensor.
$\kappa(x)$	Curvature of a beam.

ν_{12}	Layer Poisson ratio.
ν_{12f}	Carbon fiber in-plane Poisson ratio.
ν_m	PPS matrix Poisson ratio.
ν_{xy}	Blade Poisson ratio.
$\rho(x)$	Density as function of the blade length coordinate.
σ	Stress tensor.
θ	Layer rotation angle.
$\varphi_i(x)$	Mode shape.
ψ	Modal vector used in modal assurance criterion.
ω	Frequency.

Contents

1 - Introduction

In this chapter, the context of this Master thesis will be given first. This is done by introducing composites, structural health monitoring and the work of the Dynamic Based Maintenance chair, because these subjects will play an important role in this thesis. Subsequently, the theory of the rotor blade system and failure mechanics of composites are discussed. Combining this finally leads to the research questions. The chapter concludes with the thesis outline.

1.1 Context

Composites

Composite materials usually combine high strength with relatively low weight. Also, the stiffness and layout of the material is adaptable according to the design requirements. For these reasons, these materials are used in a lot of applications. For example, in rotating equipment like wind turbines and helicopter blades, and moreover, in airplanes and aerospace applications. In these applications usually high safety factors are required. An advantage of composite materials is that a large amount of damage can be present in the material before the component fails. A disadvantage is that the failure behavior is complex and the detectability is in most cases difficult. The presence of a small damage is often invisible but can, when the damage accumulates, have serious impact on the performance and life time of the structural component.

Structural health monitoring

Structural composite components are usually replaced prior to their end of life because the current condition of the material is not known exactly. By using the structural health monitoring (SHM) technology it should be possible to obtain the real condition of the component. In this way the maintenance can be done more effectively, resulting in a reduction of maintenance costs and increased operational availability.

For damage characterization a large amount of classification methods and techniques are available. It is, however, difficult to relate a specific method to the damage case at hand. Ooijevaar [1] gives an overview of the most commonly used methods and their applicability. As part of his PhD research he has explored the use of vibration analysis and the modal strain energy damage index and obtained satisfactory results on both. His research however focused on a composite aerospace structure in free-free condition. The influence of the environment and operation conditions were not taken into account.

Dynamics Based Maintenance

This assignment was performed under the chair of Dynamics Based Maintenance (DBM). The DBM chair aims to bring SHM to real life applications like, for example, the helicopter blades or wind turbines. Two master assignments have been conducted on the behavior of the rotor blade system of helicopters.

Oosterik's [2] numerical and analytic work on helicopter dynamics has provided insight on the effects of rotational and environmental factors for damage detectability. Furthermore, he tested numerically the bending stiffness distribution and its distortion as key parameter for damage. The thesis concludes that only analyzing frequency shifts is not sufficient: Mode shapes and derivatives of mode shapes should at least be included to give more insight.

Wolters [3] designed and built a demonstrator that represents the behavior of a helicopter rotor blade system. The demonstrator was used for clamped beam testing including flexible boundary conditions and multiple types of excitations. The demonstrator is currently not functioning properly and shows too much play to extract the dynamic response accurately. It however serves as a starting point for a temporary less complex test setup.

This thesis will use the topics discussed above and try to link them together. The SHM technology will be applied to detect and localize damage in a composite blade. The blade will be clamped in a helicopter-like test setup to create realistic boundary conditions. In the remaining of this section the rotor blade system will be introduced, failure mechanisms of composites will be discussed and the research questions will be stated.

1.2 Rotor blade system

This section will briefly discuss different rotor blade systems. This is done in order to understand the behavior and terminology of the earlier mentioned demonstrator. With the knowledge obtained, the functionality of different kinds of helicopter rotor blade systems can be explained. The main rotor mechanics will be discussed. This yields the different rigid and elastic degrees of freedom (DOFs) of the main rotor blade system. Finally, a short overview of the possible hinge arrangements is given.

1.2.1 Rotor mechanics

Figure 1.1 shows the typical hinge arrangement of the helicopter rotor blade system and the degrees of freedom described by Bramwell [4]. The hinges are used as a means of relieving large bending stresses at the blade root and eliminating the rolling moment which arises in forward flight. The DOFs that will be described are feathering, flapping and lagging.

Feathering

Feathering is the change of angle over the length of the blade. This motion is undesired and the torsional stiffness of the blade should be high in order to minimize this motion. The rigid feathering motion is called pitch. Pitch is the only main rotor DOF that is fully controlled by the pilot [5]. Pitch can be divided in collective and cyclic pitch. Collective pitch determines the amount of generated thrust by the blades and, therefore, the vertical movement of the helicopter. Cyclic pitch changes the lift distribution over the rotor

disk area and, therefore, controls the horizontal movement of the helicopter. Cyclic and collective pitch are controlled by the swashplates. The principle of the swashplates is shown in figure 1.2. The lower plate is non-rotating and controlled by the pilot. The remaining parts are all moving with the rotor shaft. Moving the lower plate up and down controls the collective pitch and rotating the lower plate controls the cyclic pitch. Both are controlled by the pilot.

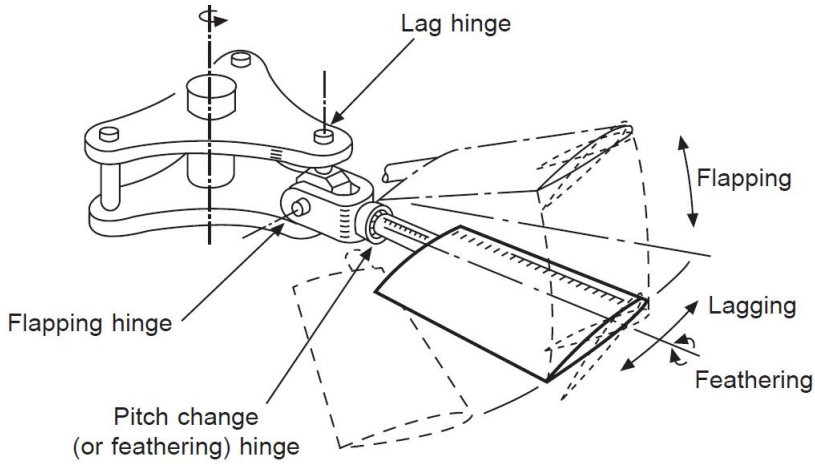

Figure 1.1: Typical hinge arrangement [4].

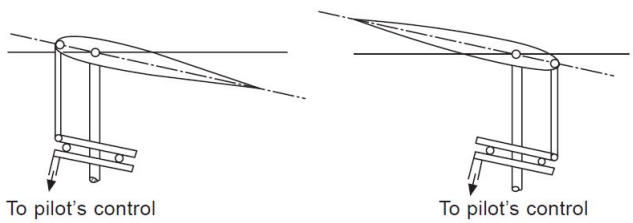

Figure 1.2: swash plates mechanism [4].

Flapping

Flapping is the motion in a plane containing the blade and the shaft. Flapping can be either rigid or elastic. The flapping motion compensates for the moments in the blade due to dissymmetry of lift in horizontal flight. The flapping hinge and rigid flapping motion are shown in figure 1.1.

Lagging

Lagging is the motion of the blade in the plane of rotation of the main rotor. The lagging motion occurs due to Coriolis moments when the blade is flapping. The lagging hinge and rigid lagging motion are also shown in figure 1.1.

1.2.2 Hinge arrangement

The three basic main rotor systems are rigid, semi-rigid and fully articulated. The distinction between these systems is made due to the way the blades are attached to the rotor hub [5].

In the rigid or hingeless rotor system the blades are rigidly connected to the rotor hub. This means that rigid flapping and lagging is not possible and the loads due to these movements should be absorbed by the hub. Most wind turbines can also be classified into this category.

The semi-rigid rotor system usually consists of two blades which are rigidly connected to the main rotor hub. The hub and blades together are free to tilt. In this way, the blades can flap as a unit. There is no lagging hinge, so lag forces should be absorbed by the hub.

The last system is the fully articulated rotor. In this system each blade is allowed to flap and lag rigidly and independently of the other blades. Due to the presence of hinges for flapping and lagging no moments are transferred to the hub. This is the most complex and costly rotor system. Helicopters are available in all of the arrangements. In all systems the pitch angle is controlled by the pilot to handle the vertical and horizontal movement of the helicopter. The demonstrator of Wolters [3] is also based on this type of rotor blade system.

1.3 Composite structures

A composite material is in its broadest definition a combination of two or more materials. In general, it combines the characteristics of these components in order to obtain properties, which could not be obtained with the separate constituents [6]. Composites are most often a combination of a polymer matrix and fiber reinforcement materials, such as carbon or glass. In this configuration fibers are used to give the material relatively high stiffness and strength with respect to the density. The matrix protects and binds the fibers together and transfers load between the fibers. The matrix and fibers can be combined in many different ways. In this way, a tailor made structure can be obtained.

In helicopters the composite materials can be used to obtain blades with high bending and torsion stiffness and a relatively low mass. Other advantages are high durability due to a high resistance against corrosion and the possibility to tailor the material properties [1].

1.3.1 Failure mechanisms

Damage yields the degradation of the composite material which can lead to failure. Composites show anisotropic mechanical properties. Because of the different strengths and orientation of the constituents, the failure behavior is also highly directional in nature. The presence of fibers and surfaces makes that even if a certain amount of cracks occur in the composite structure, it does not necessarily mean complete fracture of the structure. This is due to the cohesion between the fibers and the matrix [6]. This section will present the failure mechanisms of composite structures.

Transverse cracking

The first damage mechanism to occur is often transverse or matrix cracking. This type of crack occurs at micro level and initiates on the surface and grows parallel to the fiber in the thickness direction of the laminate. The formation of transverse cracks rarely means total fracture of a laminate. Furthermore, it does not affect the load carrying capacity of the fibers. However, because the matrix is damaged, transverse cracking does influence the mechanical and thermal properties of the laminate. The small size makes them hard to detect during inspections. The most important property of this failure mechanism is that it triggers other damage mechanisms. Figure 1.3 shows a schematic cracked laminate. The crack initiates at the free surface of the 0° layer, and grows in the thickness direction until it meets the fibers of the 90° layer.

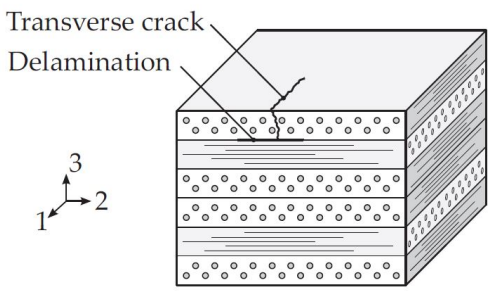

Figure 1.3: Schematic representation of transverse crack and delamination in a $[0/90/0]_s$ laminate [1].

Delamination

Chronologically, it is recognized that a delamination mostly initiates from the tip of a transverse crack. It is a crack, that runs at the interface between two layers. Therefore, this failure mechanisms occurs at meso level. Because the layers are debonding inside the material the damage is not visible on the surface of a structure. Delamination will further affect the thermal and mechanical properties of the laminate, for example its bending stiffness. Delaminations do generally not lead to complete fracture. It can, however, be the case that the component will fail, because it no longer fulfills its function. Figure 1.3 shows a delamination at the interface between the 0° and the 90° layer. This failure mechanism is particularly interesting in this thesis because SHM methods can be used to make this invisible failure mechanism visible.

Fiber failure

The most destructive kind of failure is related to fiber failure. Rracture of fibers significantly decreases the load carrying capacity of a laminate. Different types of fiber related failures can be local buckling of fibers, fiber breakage and fiber pull-out. This type of failure mechanism is not interesting in this thesis because the material is already too much damaged to be able to gain from SHM.

1.4 Research question

This research will investigate the possibility to link the damage identification of composite materials to the functionality of clamped beams with rotor blade system boundary conditions.

The research question is stated as follows:

- *To what extend can damage in a composite beam structure, subjected to rotor blade system boundary conditions, be detected with modal-based techniques while only using output data ?*

The following sub questions are formulated:

- *Can a properly working test setup with reduced complexity be obtained?*
- *Are operational modal analysis techniques suitable to detect damage in the test setup?*
- *Is there a distinction in the detectability of different composite damage scenarios?*

The modal based techniques that will be used in this assignment are modal curvature and the modal strain energy damage index. Doing so, the work of Ooijevaar [1] can be extended to more realistic applications. Furthermore, Oosterik shows that the environmental factors working on the helicopter rotor blade system are very complex [2]. Therefore, the possibility to apply the methods while using only output vibration data is considered. The test setup designed by Wolters [3] is used in the current thesis. The complexity of the test setup will be reduced. The main priority of this thesis is to design a properly working demonstrator to determine whether damage is present or not. In the future, the aim of the DBM chair is to implement SHM on the test setup representing the behavior of the fully articulating rotor blade system.

1.5 Thesis outline

The remaining of this thesis will be as follows: Chapter 2 will assess and redesign the current demonstrator. Subsequently, a composite blade is introduced and the dynamic properties of this blade are analytically determined. Chapter 3 will discuss two different modal analysis methods and the structural health monitoring methods that will be applied in this thesis. In chapter 4, the hardware and software of the experimental setup is described. Furthermore, the pristine behavior and repeatability of the used measurement system is checked. In chapter 5, the actual damage scenarios are introduced and the damage assessment is carried out. The results are given in this chapter. The thesis will end with the conclusion and discussion answering the research questions and stating possibilities for further research.

2 - Demonstrator design

This chapter will start with the assessment of an existing demonstrator setup. Next, the test setup will be redesigned according to the aim of this assignment. This means decreasing the complexity and mobility of the setup and increasing the robustness. Finally, a composite blade is introduced. The properties of this blade will be stated and calculated and the analytical dynamic bending properties of the new setup will be derived.

2.1 Original test setup

In a previous master assignment, a setup is build with the aim to simulate the behavior of a fully articulated helicopter rotor blade system [3]. A 3D model of the most important part of this demonstrator is shown in figure 2.1.

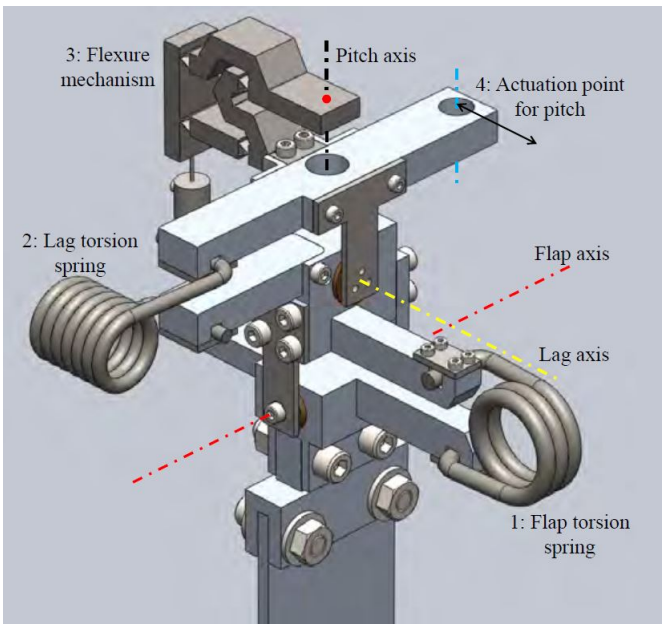

Figure 2.1: Original demonstrator [3].

In this figure, the flapping, lagging, and feathering axis are indicated with red, yellow, and black dotted lines. Furthermore, torsion springs are implemented to generate rotational stiffness in the flap and lag hinge. This stiffness is necessary to realize the desired ratio between the rigid and first elastic natural frequency to simulate the behavior of the

rotor blade system. The actuation of this system is done with a voice coil motor (VCM) to actuate cyclic pitch and a shaker on the flexure mechanism to actuate flap.

Wolters concludes that the lag and pitch hinge of the demonstrator show too much play and, therefore, it is not possible to determine the dynamic properties of the test setup. Furthermore, he concludes that actuation with the flexure and the VCM was not performing like expected [3].

2.2 Redesign Demonstrator

Before a redesign can be proposed, the objectives should be clear first. The first aim of this redesign is to obtain a properly working experimental setup. Because the lag and pitch hinges show a lot of play, these active degrees of freedom are removed from the setup. Doing so, the noise level should decrease and the accuracy of the system should be enhanced. Furthermore, flapping is the most easy degree of freedom to measure, so this will be a good starting point for the less complex demonstrator. The second aim is to investigate the influence of the torsion spring on the dynamic response of the blade. As mentioned earlier, the focus of this research is on boundary conditions that are typical for rotor blade system applications. These different boundary conditions can be simulated by applying different torsion springs at the flapping hinge. In this way, for example, a hinged system can be obtained by removing the spring. The level of noise and vibration response will change with different boundary conditions and therefore the damage detectability of both cases will be explored.

The next step comprises the actual redesign of the demonstrator. First, the lag and pitch hinges will be removed. In this way, the demonstrator will be able to show only a flapping motion excited by a shaker at the root of the blade. As discussed earlier, the torsional spring at the bending degree of freedom will stay in the assembly. The adjusted demonstrator is shown in figure 2.2. It can be seen that the demonstrator could be adjusted with relatively small changes. The flapping hinge is mounted directly to the frame. This is done in such a way the demonstrator can always be turned back towards the original situation.

2.3 Composite blade

A composite plate is obtained from the Thermoplastic composite research center (TPRC). The plate consists of carbon fibers and poly-phenylene sulfide (PPS) matrix material. The name of the composite material is C/PPS 5hs T300JB 3000-40B from Torayca [7]. It consists of four layers of 5 harness satin (5hs) weaves in $[0/90_2]_s$ configuration. This weave form is generally used because it is very flexible. It is characterized by the fact that the fill yarn floats over four warp yarns and then under one. Out of this plate, the test specimens are obtained. In table 2.1 some important fiber, matrix, and blade properties are listed. In the following subsections, first some material properties of the blade are calculated with the classical lamination theory. Finally, bending frequencies and mode shapes as function of the torsional stiffness can be determined.

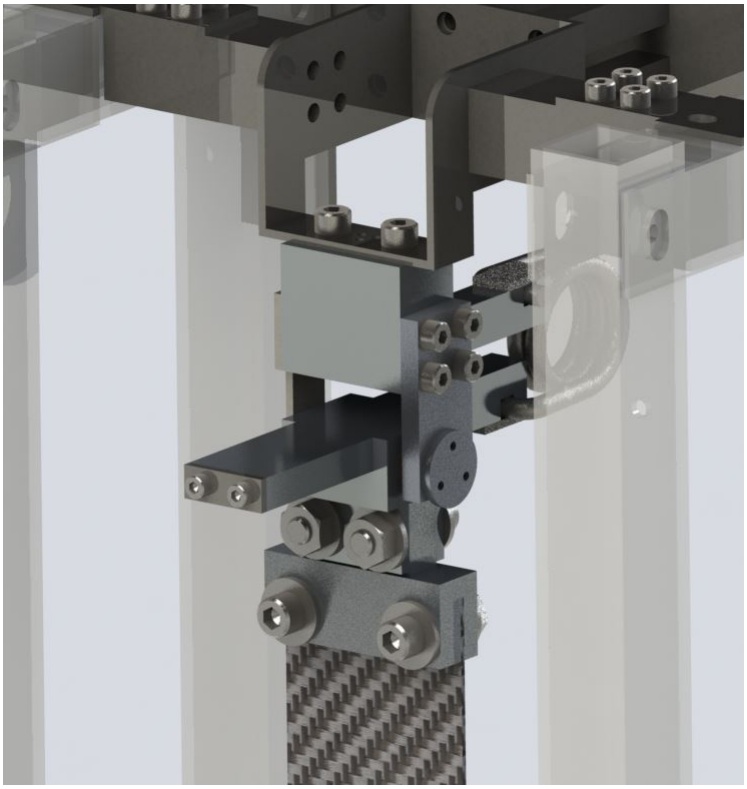

Figure 2.2: Adjusted demonstrator design.

Table 2.1: Composite blade properties.

Carbon fibers [8]			**PPS matrix** [6]			**Blade dimensions**		
E_{1f}	230	GPa	E_m	4	GPa	L	0.45	m
E_{2f}	20	GPa				w	0.05	m
G_{12f}	9	GPa	G_m	1.5	GPa	t	0.0012	m
ν_{12f}	0.2		ν_m	0.35				

2.4 Composite blade properties

To be able to calculate the blade mechanical properties, the woven layers are divided in two unidirectional layers with half thickness. This means that the laminate is an assembly of eight unidirectional, instead of four woven, layers. First the elasticity moduli, shear modulus and Poisson ratio of one layer with the principle directional along the fibers are calculated which can then be assembled in the layer stiffness matrix. The longitudinal modulus can be obtained by the rule of mixture; the transverse modulus with the parallel-series model; the shear modulus with the inverse rule of mixture; and the Poisson ratio with the rule of mixture [6]. These parameters are shown in equation (2.1) - (2.4).

$$E_1 = E_m v_m + E_{1f} v_f \tag{2.1}$$

$$E_2 = (1 - \sqrt{v_f})E_m + \frac{\sqrt{v_f} E_m E_{2f}}{v_f E_m + \sqrt{v_f}(1 - \sqrt{v_f})E_{2f}} \tag{2.2}$$

$$G_{12} = (\frac{v_m}{G_m} + \frac{v_f}{G_{12f}})^{-1} \tag{2.3}$$

$$\nu_{12} = \nu_m v_m + \nu_{12f} v_f \tag{2.4}$$

In these equations v_f and v_m are the fiber and matrix volume fraction. These are estimated by calculating the mass of the fibers with respect to the mass of a blade. The total weight of one blade is 41 gram. The weight of one fabric layer is 198 g/m^2 [7]. Taking into account the blade dimensions and the fact that there are four layers, the fiber fraction is calculated to be 43 %.

It should be noted that the shear modulus is often found to be too low in the definition of equation (2.3). Next, the stress-strain relationship of one composite layer will be determined. When assuming a plane state of stress and orthotropic layers, this relation is shown in equation (2.5). In this equation $[C]$ is called the stiffness matrix.

$$\begin{Bmatrix} \sigma_1 \\ \sigma_2 \\ \sigma_6 \end{Bmatrix} = \begin{bmatrix} \frac{E_1}{1-\nu_{12}\nu_{21}} & \frac{\nu_{21}E_1}{1-\nu_{12}\nu_{21}} & 0 \\ \frac{\nu_{21}E_1}{1-\nu_{12}\nu_{21}} & \frac{E_2}{1-\nu_{12}\nu_{21}} & 0 \\ 0 & 0 & G_{12} \end{bmatrix} \cdot \begin{Bmatrix} \varepsilon_1 \\ \varepsilon_2 \\ \varepsilon_6 \end{Bmatrix} \quad or \quad \{\sigma\} = [C] \cdot \{\varepsilon\} \tag{2.5}$$

In this equation the shear tensor component is defined as $\varepsilon_6 = \frac{1}{2}\gamma_{12}$. The Poisson ratio ν_{21} follows from the symmetry of the stiffness matrix. The stiffness matrix changes from the local to the global coordinate system by an in-plane rotation of the layer. The transformed stiffness matrix $[C^*]$ is defined as follows:

$$[C^*] = [T]^{-1} \cdot [C] \cdot [R] \cdot [T] \cdot [R]^{-1} \tag{2.6}$$

In this equation $[R]$ is the so-called Reuter matrix and $[T]$ the transformation matrix. The Reuter matrix is necessary to compensate for the difference between the engineering shear component γ_{12} and the shear deformation tensor component ε_6, as stated earlier. In case of plane stress and rotation over an angle θ these matrices are defined as:

$$[R] = \begin{bmatrix} 1 & 0 & 0 \\ 0 & 1 & 0 \\ 0 & 0 & 2 \end{bmatrix} \tag{2.7}$$

$$[T] = \begin{bmatrix} \cos^2\theta & \sin^2\theta & -2\cos\theta\sin\theta \\ \sin^2\theta & \cos^2\theta & 2\cos\theta\sin\theta \\ \cos\theta\sin\theta & -\cos\theta\sin\theta & \cos^2\theta - \sin^2\theta \end{bmatrix}^{-1} \tag{2.8}$$

The classical lamination theory can be used to calculate the properties of laminated beams consisting of multiple, unidirectional, layers. First, the laminate extensional stiffness matrix is calculated. In this matrix the strains in the laminate are related to the external forces. This matrix can be calculated as follows:

$$A_{ij} = \sum_{k=1}^{N} (C^*_{ij})(z_k - z_{k-1}) \tag{2.9}$$

In equation (2.9), N is the number of layers, C^* is the layer stiffness matrix, and z_k and z_{k-1} indicate the thickness of the layer measured from the laminate mid-plane. To be able to calculate the mechanical properties, the inverse relation is necessary. Because the laminate is symmetric in this case, the extensional compliance matrix $[a]$ is equal to the inverse stiffness matrix $[A]^{-1}$. When h is the laminate thickness and $[a]$ is defined as:

$$[a] = \begin{bmatrix} a_{11} & a_{12} & a_{16} \\ a_{21} & a_{22} & a_{26} \\ a_{61} & a_{62} & a_{61} \end{bmatrix} \tag{2.10}$$

The mechanical properties can be calculated with the following equations:

$$E_x = \frac{1}{h \cdot a_{11}} \tag{2.11}$$

$$E_y = \frac{1}{h \cdot a_{22}} \tag{2.12}$$

$$G_{xy} = \frac{1}{h \cdot a_{66}} \tag{2.13}$$

$$\nu_{xy} = -\frac{a_{21}}{a_{11}} \tag{2.14}$$

In table 2.2 the values of the properties discussed above are given. It can be seen that with the current fiber orientation, the elasticity moduli are in the same order of magnitude as the aluminum blade. The magnitude of the shear modulus of the composites is, however, only about one tenth of an aluminum value. This confirms once more that the fiber orientation in composite blades is very important and that the properties are highly direction dependent.

Table 2.2: Mechanical blade properties.

	$[0/90_2]_s$	
E_x	49.3	GPa
E_y	49.3	GPa
G_{xy}	2.1	GPa
ν_{xy}	0.29	

2.5 Bending blade vibrations

The mechanical properties calculated in the previous section will now be used to determine the dynamic mode shapes and eigenfrequencies of the test setup. The setup is schematically shown in figure 2.3. The torsional stiffness will be indicated with the symbol c.

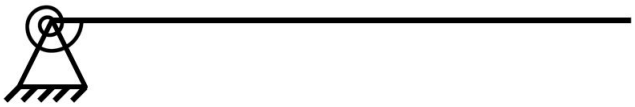

Figure 2.3: Schematic overview bending blade situation.

The partial differential equation of motion of bending reads [10]:

$$\rho(x)\frac{\partial^2 y(x,t)}{\partial t^2} = -\frac{\partial^2}{\partial x^2}\left[EI(x)\frac{\partial^2 y(x,t)}{\partial x^2}\right] + f(x,t) \tag{2.15}$$

In equation (2.15), $y(x,t)$ is the transverse displacement of the blade, $\rho(x)$ is the mass per unit length, $EI(x)$ the bending stiffness, and $f(x,t)$ a distributed bending load. Taking the external load zero, $\rho = m/L$, and bending stiffness constant of the length over the blade the spatial part of the differential equation of motion for transverse vibrations can be obtained by separation of variables. The solution is shown in equation (2.16).

$$\frac{d^4Y(x)}{dx^4} - \frac{m\omega^2}{EIL}Y(x) = 0 \quad \rightarrow \quad \frac{d^4Y(x)}{dx^4} - \beta^4 Y(x) = 0, \quad \beta^4 = \frac{m\omega^2}{EIL} \tag{2.16}$$

The general solution to this fourth order problem is:

$$Y(x) = B_1\cos(\beta x) + B_2\sin(\beta x) + B_3\cosh(\beta x) + B_4\sinh(\beta x) \tag{2.17}$$

The constants B_1 to B_4 can be solved using the following four boundary conditions. The first two boundary conditions are at the hinged torsion spring end and the last two at the free end. The second equation shows the added moment at the hinge due to the torsion stiffness c.

$$Y(0) = 0 \qquad \text{(Zero displacement)} \tag{2.18}$$

$$EI\left.\frac{d^2Y(x)}{dx^2}\right|_{x=0} + c\left.\frac{dY(x)}{dx}\right|_{x=0} = 0 \qquad \text{(Zero bending moment)} \tag{2.19}$$

$$\left.\frac{d^2Y(x)}{dx^2}\right|_{x=L} = 0 \qquad \text{(Zero bending moment)} \tag{2.20}$$

$$\left.\frac{d^3Y(x)}{dx^3}\right|_{x=L} = 0 \qquad \text{(Zero shear force)} \tag{2.21}$$

The derivatives of Y(x) are:

$$\frac{dY(x)}{dx} = \beta(-B_1\sin(\beta x) + B_2\cos(\beta x) + B_3\sinh(\beta x) + B_4\cosh(\beta x)) \tag{2.22}$$

$$\frac{d^2Y(x)}{dx^2} = \beta^2(-B_1\cos(\beta x) - B_2\sin(\beta x) + B_3\cosh(\beta x) + B_4\sinh(\beta x)) \tag{2.23}$$

$$\frac{d^3Y(x)}{dx^3} = \beta^3(B_1\sin(\beta x) - B_2\cos(\beta x) + B_3\sinh(\beta x) + B_4\cosh(\beta x)) \tag{2.24}$$

Filling in the boundary conditions yield:

$$B_1 + B_3 = 0 \quad \rightarrow \quad B_1 = -B_3 \tag{2.25}$$

$$EI\beta^2(-B_1 + B_3) + c\beta(B_2 + B_4) = 0 \tag{2.26}$$

$$\beta^2(-B_1\cos(\beta L) - B_2\sin(\beta L) + B_3\cosh(\beta L) + B_4\sinh(\beta L)) \tag{2.27}$$

$$\beta^3(B_1\sin(\beta L) - B_2\cos(\beta L) + B_3\sinh(\beta L) + B_4\cosh(\beta L)) \tag{2.28}$$

The first condition can be substituted into the other three equations and written in matrix-vector notation. This is shown in equation (2.29).

$$\begin{bmatrix} c\beta & 2EI\beta^2 & c\beta \\ -\beta^2\sin(\beta L) & \beta^2(\cos(\beta L) + \cosh(\beta L)) & \beta^2\sinh(\beta L) \\ -\beta^3\cos(\beta L) & \beta^3(-\sin(\beta L) + \sinh(\beta L)) & \beta^3\cosh(\beta L) \end{bmatrix} \begin{Bmatrix} B_2 \\ B_3 \\ B_4 \end{Bmatrix} = \begin{Bmatrix} 0 \\ 0 \\ 0 \end{Bmatrix} \tag{2.29}$$

The non-trivial solution can be found by setting the determinant of the matrix to zero. This yields an equation for β with an infinite number of solutions. Note that the solution of this problem will also depend on the torsional stiffness c. Working out the determinant yields:

$$\begin{aligned} &c\beta^6(\cos(\beta L)\cosh(\beta L) + \cosh^2(\beta L) + \sin(\beta L)\sinh(\beta L) - \sinh^2(\beta L)) \\ &+ 2EI\beta^7(\sin(\beta L)\cosh(\beta L) - \cos(\beta L)\sinh(\beta L)) \\ &+ c\beta^6(\sin^2(\beta L) - \sin(\beta L)\sinh(\beta L) + \cos^2(\beta L) + \cos(\beta L)) = 0 \end{aligned} \tag{2.30}$$

Equation (2.30) can be rearranged and divided by β^6. This gives the following characteristic equation:

$$\begin{aligned} &c\cdot\cos^2(\beta L) + c\cdot\cosh^2(\beta L) + c\cdot\sin^2(\beta L) - c\cdot\sinh^2(\beta L) + 2c\cdot\cos(\beta L)\cosh(\beta L) \\ &- 2EI\beta\cos(\beta L)\sinh(\beta L) + 2EI\beta\sin(\beta L)\cosh(\beta L) = 0 \end{aligned} \tag{2.31}$$

Taking zero stiffness ($c = 0$ Nm/rad) reduces equation (2.31) to the characteristic equation for the hinged situation and taking a large stiffness gives the clamped solution. When the characteristic equation is zero, the value for β can be determined for a certain stiffness. The eigenfrequencies can be found by rewriting equation (2.16). This gives the following equation:

$$\omega = (\beta L)^2\sqrt{\frac{EI}{mL^3}} \tag{2.32}$$

In order to draw the mode shapes, the values obtained in equation (2.32) should be substituted into the matrix-vector product in equation (2.29). One of the constants should be assumed. In this way the dependency of the constant can be determined and the mode

shapes can be plotted. Note that the above stated implicates that the amplitude of the mode shapes is scaled.

Table 2.3 shows the bending frequencies of the different blade configurations with different spring stiffness. Later in this thesis the measurement equipment will be discussed. Strain sensors will be used to measure the response of the blade. Because the strain will be measured, it is convenient to also determine the mode shapes in terms of the strain. These mode shapes can be obtained by differentiating twice the displacement mode shapes. The strain shapes are shown in figure 2.4. The first eight mode shapes are considered in this analysis. This is done, because it is assumed that higher mode shapes cannot be found with the used discrete sensor network. The extreme cases are considered: the clamped and the hinged configuration.

Later in this thesis the analytical strain shapes will be used to verify the behavior of the experimental setup. The behavior of the two cases, with and without torsion spring, should lie within the given extremes.

Table 2.3: Eigenfrequencies of the composite blade in [Hz].

Mode shape number	**0/90 (hinged)** $c \approx 0$ **[Nm/rad]**	**0/90 (clamped)**— $c \approx \infty$
1	23.4	5.2
2	76.3	33.5
3	158.1	93.7
4	271.2	184.3
5	414.6	305.1
6	588.3	454.0
7	792.4	635.1
8	1023.2	846.5

2.6 Closing remarks

This chapter discussed the redesign of an existing, not correctly functioning test setup. Furthermore, a composite blade was introduced and the properties of this blade were calculated with the classical lamination theory. Finally, the mode shapes and natural frequencies of the test setup were analytically calculated. The mode shapes and frequencies will also be determined experimentally later in this thesis and compared with the properties shown in this chapter.

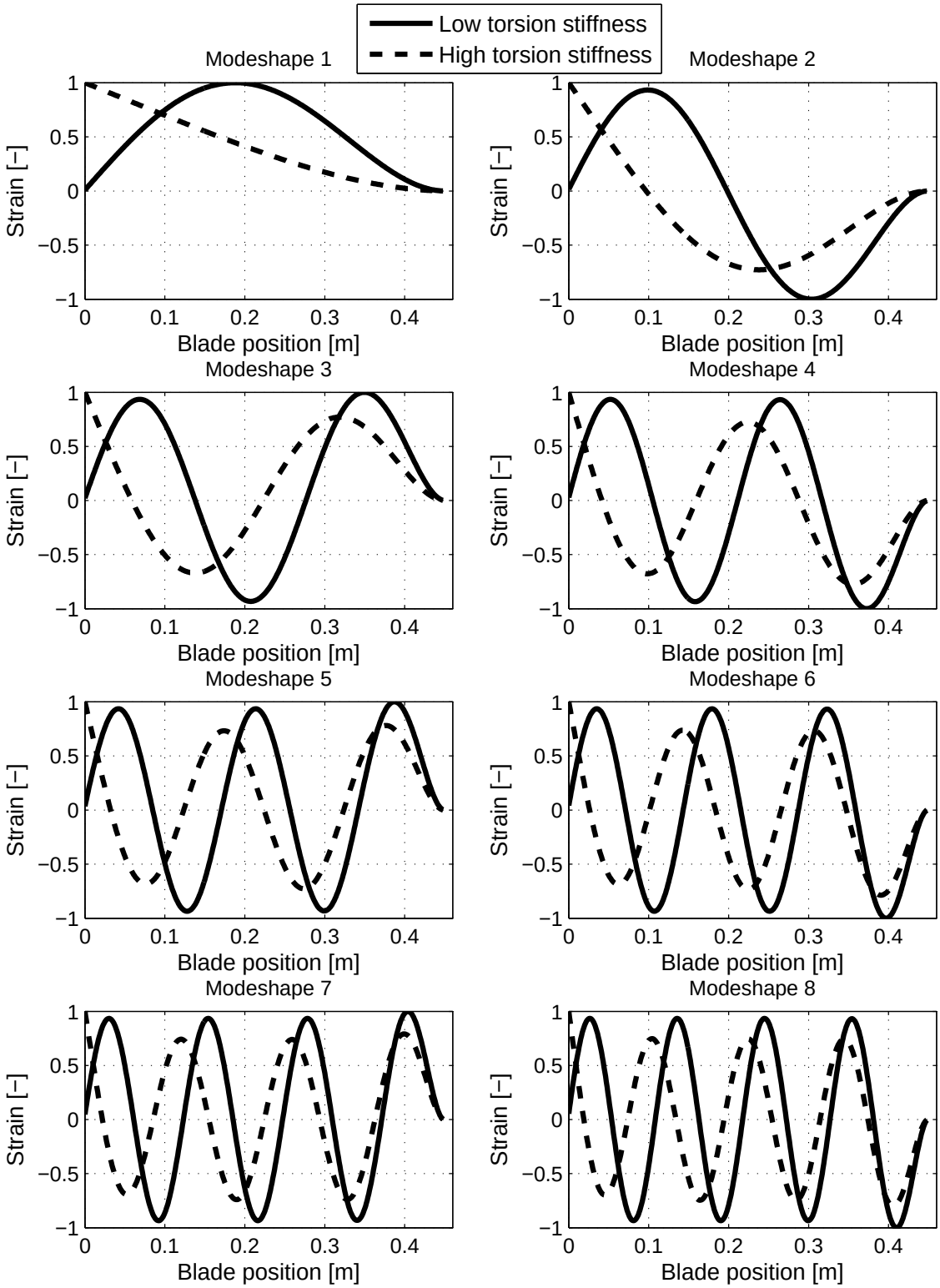

Figure 2.4: First eight strain mode shapes of the composite blade with low torsion stiffness (hinged) and high torsion stiffness (clamped).

3 - Structural Health Monitoring theory

Several techniques are available for non destructive testing. Some of these are visual inspection, ultrasonic methods, acoustic emission, and vibration based methods. According to Rytter [11], the different methods for damage identification can be divided into four levels :

- Level 1: The method gives a qualitative indication that damage is present in the structure. (Detection)
- Level 2: The method gives information about the probable location of the damage. (Localization)
- Level 3: The method gives information about the size of the damage. (Severity)
- Level 4: The method gives information about the remaining useful life for the structure given a certain damage state. (Prognosis)

The detection, localization, and severity indication are called diagnostics. The focus of the current thesis is on these levels. As mentioned earlier in this report, the modal curvature damage index (MC-DI) and modal strain energy damage index (MSE-DI) are applied in this thesis. Both are vibration based methods. A disadvantage of these methods is the relatively low sensitivity to small damages. Very small damages, such as transverse cracking, cannot be identified. However, as indicated earlier the focus of this thesis is on delamenation damages. It should be possible to assess these with the mentioned methods. Advantages are easy data interpretation and easy application for SHM. Moreover, vibration based methods are global methods, which can be used either passively or actively. This means it should be able to assess the whole blade with ambient vibrations.

For SHM generally a network of sensors is used. In this thesis piezo sensors are mounted on the blade. These sensors are used because they are cheap and easy to mount on the blade. Furthermore, as will be indicated later in this chapter, strains are used in both SHM methods. When the measured values can be used directly the measurement time will be less. The measurement grid and specifications of the sensors will be discussed in chapter 4.

Different studies show that both methods should be able to detect, localize and probably also assess the severity of the damage. The MC-DI is applied to a numerical test beam by Ooijevaar [1] and Oosterik [2]. Both show satisfactory results, it should however be expected to be more difficult to get the same results in an experimental setup. The numerical method is an ideal situation. In real life there will always be more noise from

the environment and the mounting parts. Furthermore, the measurement equipment will introduce some noise. The MSE-DI is tested in experimental setups by Ooijevaar [1] and Cornwell [14]. Both show very promising results.

In this chapter the techniques behind the two SHM methods are explained. Both methods use the mode shapes of the blade as input parameter. These mode shapes can be extracted from the measurement data with either the Engineering Modal Analysis (EMA) or the Operational Modal Analysis (OMA). The basic different between these two methods comes from the fact the EMA uses input and output data while OMA only uses output data. The aim of this thesis is to use only output vibration data. This would be a major difference with the studies discussed above. Before the structural health methods can be explained first the EMA and OMA methods are explained.

3.1 Modal Analysis methods

As explained earlier, two methods will be applied to determine the mode shapes. An overview of both methods is shown in figure 3.1. In the next section the theory of EMA will be described. Subsequently, the theory of OMA will be discussed.

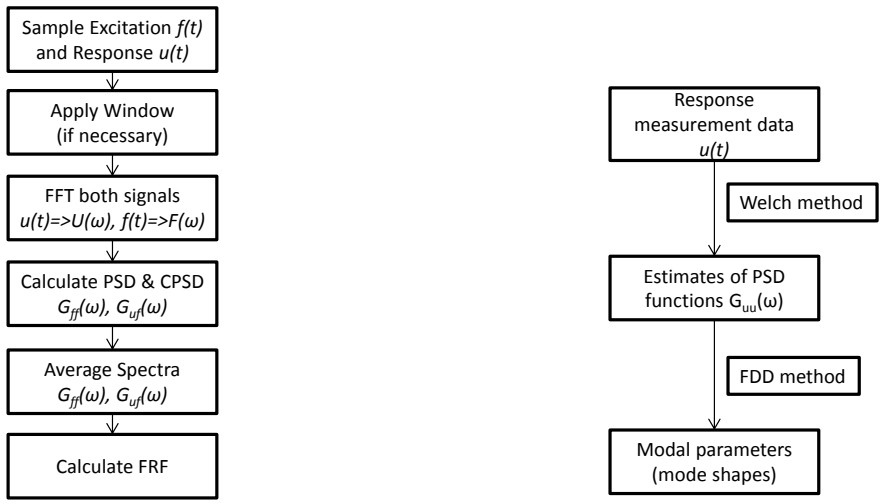

Figure 3.1: Schematic overview of the EMA (left) and OMA (right) method.

3.1.1 Engineering Modal Analysis

EMA is the modal analysis technique where the dynamic properties of structures are obtained by active excitation of the structure. The EMA technique is among others described by Schwarz [15] and Tijdeman [16].

Experimental modal parameters, like eigenfrequencies and mode shapes, are obtained from a set of Frequency Response Function (FRF) measurements. In a broad sense, the FRF describes the input-output relationship between two points on a structure as a function of frequency. The mode shapes of a structure are given by plotting the operational

deflection shapes (FRF) at the corresponding eigenfrequency. A schematic overview of the process from measurement data to FRF is given at the left side of figure 3.1.

The process starts with obtaining the input and output vibration data at discrete locations during a given time interval. In order to prevent aliasing the time signals should be sampled with a frequency of at least two times the frequency one is interested in (Nyquist frequency). Subsequently, the time signals are cut into equal time blocks with a certain overlap. The second step is the application of a window. The window is used to reduce leakage. Leakage occurs when the time signal shows jumps at the begin and end of the signal. As a result, energy is leaked to other frequencies. To prevent leakage a window can be applied which makes the signal zero towards the edges. A often used window is the Hanning window. A example of the application on a random time signal is shown in figure 3.2. The time signal should be corrected for the loss of energy due to the window. This can be done by dividing the resulting spectrum by the energy content of the window function, as shown in equation (3.1). In this equation N is the number of discrete time steps in the window function and w_r is the amplitude at every time step.

$$\frac{1}{N}\sum_{r=0}^{N-1} w_r^2 \tag{3.1}$$

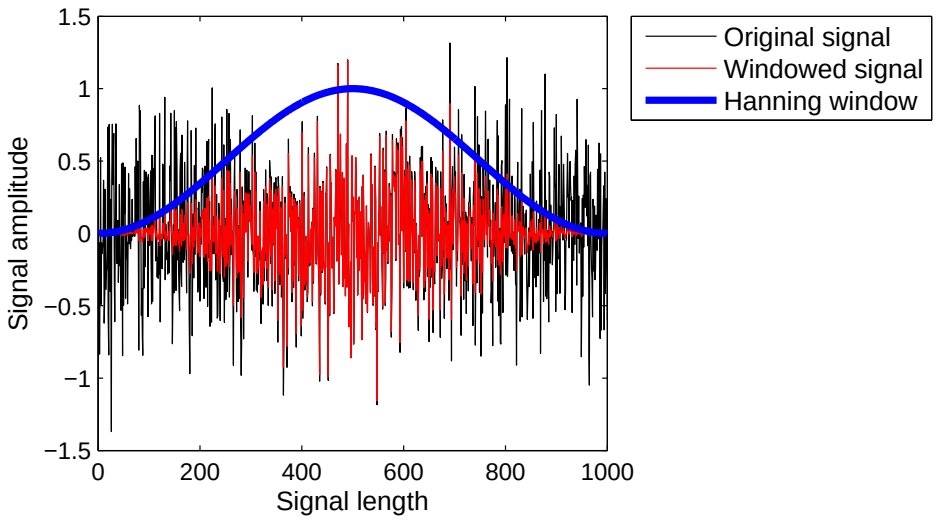

Figure 3.2: Hanning window applied at a random signal.

The next step is the transformation of the input and output time signals to the frequency domain. This can be done with the fast Fourier transform. For this transformation the number of values per sample should be a power of two. If the length of the signal is less then this power of two it is padded with zeros. In the frequency domain, the importance of using a window is shown by the two FRFs in figure 3.3. It can be seen that the window reduces the noise and makes the FRF a lot more smooth.

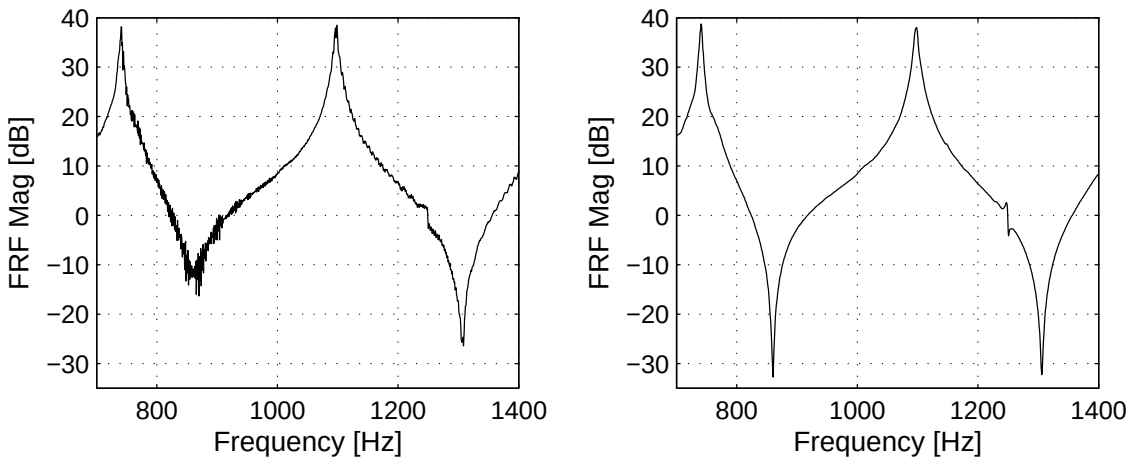

Figure 3.3: FRF without (left) and with (right) Hanning window.

An averaging process can be carried out to increase the accuracy and statistical reliability of the measurement. The input and output frequency domain data of more than one measurement can be averaged with a certain overlap with the aim to make the used data more reliable.

Finally, the FRF can be calculated. As mentioned earlier, the FRF was defined as the ratio of the Fourier transforms of the output and input signal. In order to remove noise and non-linearities both the numerator and denominator can be multiplied by the complex conjugate of the Fourier transformed input signal as shown in equation (3.2).

$$H(\omega) = \frac{U(\omega) \cdot F^*(\omega)}{F(\omega) \cdot F^*(\omega)} = \frac{G_{UF}}{G_{FF}} \tag{3.2}$$

In this equation, $U(\omega)$ is the Fourier transform of the output signal and $F(\omega)$ the Fourier transform of the input signal. The numerator and denominator in equation (3.2) are called respectively the cross power spectral density (CPSD) and auto power spectral density (PSD). The auto power spectral density and cross power spectral density are defined as the Fourier transform of respectively the auto-correlation and cross-correlation function. The auto power spectral density describes how the average energy is distributed over the different frequencies. The cross power spectral density describes the average energy over the different frequencies shared by two signals.

The eigenfrequencies can be obtained by summing the FRFs of all discrete measurement points and determine where the peaks of the plot are. The mode shapes can subsequently be obtained by plotting the magnitude of the corresponding FRFs of every point at these eigenfrequencies.

3.1.2 Operational Modal Analysis

OMA is the modal analysis technique that can be used to identify modal properties of a structure using vibration data collected under operational conditions. The OMA technique is described by Schiphorst [12], Welch [13] and Brincker [17].

A lot of methods can be used to obtain the modal parameters with OMA. A short overview of the available methods is given by Schiphorst [12]. This thesis will apply the

Welch method and Frequency Domain Decomposition (FDD) method. This is done because this method of determining the modal parameters is fast and intuitive. Furthermore, the method is capable of detecting closely spaced and even repeated modes. A schematic overview of the process from response measurement data to modal parameters is given at the the right side of figure 3.1.

The most important difference between this method and the EMA method described above is that the PSD functions are in this method calculated using only output data and with respect to the other sensors. The EMA method is using both input and output data and PSD functions are calculated with respect to the input force.

Welch Method

The first step is to convert the measured output vibration data into estimated values of the PSD functions. This can be done with the method described by Welch [13]. First, the output signal is again cut into time blocks with a certain overlap like in the EMA method. Each block is again windowed and transformed to the frequency domain by taking the Fourier transform. Subsequently, the PSD estimate can be obtained by averaging the Fourier transforms.The method described above results in a 2D matrix for every discrete frequency step with the estimated PSD function of every discrete measurement point on its diagonal. The off-diagonal term are the estimated CPSD functions of every measurement location to all the other locations.

FDD method

The theoretical background of the FDD method is based on the relationship between the input and output measurement data, respectively $f(t)$ and $u(t)$:

$$G_{uu}(\omega) = H^*(\omega)G_{ff}(\omega)H(\omega)^T \tag{3.3}$$

In which $G_{ff}(\omega)$ and $G_{uu}(\omega)$ are respectively the input and output PSD matrices. $H(\omega)$ is the FRF matrix and the superscripts $*$ and T denote the complex conjugate and the transpose, respectively.

When the input measurement data is assumed to be white noise, the input PSD is a constant matrix $G_{ff}(\omega) = C$. If it is also assumed that the damping of the system is light. It can be shown that, at a certain frequency ω, only a limited number of modes will contribute significantly.

In the previous subsection the Welch method was used to compute the estimated output PSD matrix $\widehat{G}_{uu}(\omega_i)$ at discrete frequencies $\omega = \omega_i$. These can be decomposed into a set of auto spectral density functions, each corresponding to a single degree of freedom system. This can be done by taking the Singular Value Decomposition:

$$\widehat{G}_{uu}(\omega_i) = U_i S_i U_i^H \tag{3.4}$$

In which U_i is a normalized matrix holding the singular vectors u_{ij} and S_i is a diagonal matrix holding the scalar singular values s_{ii}. The eigenfrequencies of the system can be found by plotting the singular values as a function of the frequency. The peaks in this plot correspond to the eigenfrequencies of the system. In the case only one mode is dominating the first singular vector will be a lot higher then the second one. If this is the case the first singular vector u_{i1} is an estimate of the mode shape and can therefore be plotted as a

function of the beam coordinates. The performance of both the EMA and OMA method will be compared in the next chapter.

3.2 Structural Health Monitoring methods

Due to damage, the modal parameters of a structure change. In the previous subsections two methods that can be used to determine the natural frequencies and corresponding mode shapes are introduced. By comparing the modal parameters of the damaged and undamaged blade it should be possible to say something about the detection, localization and severity of damage. Drawbacks are, however, the global character of the natural frequencies and low sensitivity to damage of the mode shapes. A better approach is using derivatives of mode shapes [18]. The two methods described below both use derivatives of mode shapes as input parameter.

3.2.1 Modal curvature damage index

Mode shape curvatures are found to be sensitive to small perturbation and therefore, they will be used in this thesis.

The curvature of a beam at location x of the blade can be described as:

$$\kappa(x) = \frac{M(x)}{EI(x)} \tag{3.5}$$

In this equation $M(x)$ and $EI(x)$ are the applied bending moment and flexural rigidity. From this equation it can be seen that damage, normally associated with a local reduction of stiffness, will lead to a local increase in curvature. By comparing the curvature of the damaged and undamaged mode shapes the existence and extend of damage can be measured.

Piezo strain elements will be used to measure the strain at the surface in the length direction of the blade. The strain at the surface is defined in equation (3.6), where u is the displacement of the blade in length direction. For this method the curvature of the blade is considered. The curvature is defined as in equation (3.7), where w is the displacement perpendicular on the blade.

$$\varepsilon = \left.\frac{\partial u}{\partial x}\right|_{z=\frac{t}{2}} \tag{3.6}$$

$$\kappa = \frac{\partial^2 w}{\partial x^2} \tag{3.7}$$

The relation between the strain and the curvature is given by:

$$\kappa = \frac{2\varepsilon}{t} \tag{3.8}$$

In this equation t is the thickness of the blade. It can be seen that the curvature and strain of the blade only differ by a constant. Therefore, the measured values can be used to apply this method.

The blade is now divided into N elements in length direction. The curvature in element j can be calculated. At a certain location where damage is present the value of the mode

shape curvature will be significantly higher than at other locations. This location can be characterized by calculating the curvature difference values. The modal curvature damage index can be calculated as follows:

$$\Delta_j = |\widetilde{\kappa}_j(x)| - |\kappa_j(x)| \tag{3.9}$$

Based on the curvature difference values of the damaged ($\widetilde{\kappa}_j(x)$) and reference ($\kappa_j(x)$) blade the location of damage in the structure can be identified. It is should also be possible to sum the damage indexes of more than one mode shape with the aim to obtain more reliable results.

3.2.2 Modal strain energy damage index

The second SHM method is based on the change in strain energy in an element between a reference and damaged state. An advantage of this method is that information of several modes can be combined in order to determine the location and severity of the damage. The damage can both be derived for 1D beam and 2D plate like applications. Ooijevaar [1] shows that, when rows of sensors in bending direction are used, the 1D method shows more consistent and satisfying results. This is because there a lot of more change in strain over the length of the blade than over the width. Therefore, the 1D beam method will be derived in this section. In the following the theory will be described as originally presented by Stubbs [19] and reproduced with help of the thesis of Schiphorst [12] and Cornwell [14]. The general definition of the strain energy is as follows:

$$U = \frac{1}{2}\int_V \sigma\varepsilon dV \tag{3.10}$$

The bending modes of the blades will be most important. Therefore, only the bending strain will be taken into account. The strain distribution for a beam subjected to pure bending is linear over the thickness of the blade. As mentioned earlier piezo strain elements will be used to measure the strain at the surface of the blade. To describe the bending strain energy the measured stain at the surface should be multiplied with a term to make it dependent of the thickness coordinate z. The bending strain is shown in equation (3.11).

$$\varepsilon_x = \left.\frac{\partial u}{\partial x}\right|_{z=\frac{t}{2}} \cdot \frac{2z}{t}, \qquad z \in \left[-\frac{t}{2}, \frac{t}{2}\right] \tag{3.11}$$

$$\sigma_x = E_{xx}\varepsilon_x \tag{3.12}$$

Equation (3.12) is also known as Hook's law. Substituting equations (3.11) and (3.12) into equation (3.10) gives:

$$U = \frac{1}{2}\int_V E_{xx}\left(\left.\frac{\partial u}{\partial x}\right|_{z=\frac{t}{2}} \cdot \frac{2z}{t}\right)^2 dV \tag{3.13}$$

The volume integral in equation (3.13) can be divided into two integrals:

$$U = \frac{1}{2}\int_0^l \frac{4E_{xx}}{t^2}\int_A z^2 dA\left(\left.\frac{\partial u}{\partial x}\right|_{z=\frac{t}{2}}\right)^2 dx \tag{3.14}$$

The area integral gives the area moment of inertia. the following formula for the energy can be obtained:

$$U = \frac{1}{2}\int_0^l \frac{4E_{xx}I_{zz}}{t^2}\left(\left.\frac{\partial u}{\partial x}\right|_{z=\frac{t}{2}}\right)^2 dx \tag{3.15}$$

Now, the normalized amplitude of a certain bending mode shape $\varphi_i(x)$ is considered. Also, the thickness of the blade is considered constant over the length. The energy associated with that mode shape is:

$$U_i = \frac{2}{t^2}\int_0^l E_{xx}I_{zz}\left(\frac{\partial \varphi_i}{\partial x}\right)^2 dx \tag{3.16}$$

The blade is now divided into N elements in length direction. For the mode shape amplitude $\varphi_i(x)$ the strain energy in element j is defined as:

$$U_{ij} = \frac{2}{t^2}\int_{x_{j-1}}^{x_j} (E_{xx}I_{zz})_j\left(\frac{\partial \varphi_i}{\partial x}\right)^2 dx \tag{3.17}$$

Now, equation (3.16) and (3.17) can be combined to calculate the fraction of energy F_{ij} in a certain element with respect to the total blade. The fractional energy for a certain mode shape in an element is defined as:

$$F_{ij} = \frac{U_{ij}}{U_i} \tag{3.18}$$

The same derivation can be done for a damaged blade. In the remaining of this section the damage parameters will be indicated with a tilde sign. If it is assumed that the damage is located at a small number of elements and the flexural rigidity is constant over an element then the fractional energy remains relatively constant in the intact elements, $F_{ij} = \widetilde{F}_{ij}$. For the element j and mode i the following relation can than be derived:

$$\left(\frac{2E_{xx}I_{zz}}{t^2}\right)_j \int_{x_{j-1}}^{x_j}\left(\frac{\partial \varphi_i}{\partial x}\right)^2 dx/U_i = \left(\frac{2\widetilde{E_{xx}I_{zz}}}{t^2}\right)_j \int_{x_{j-1}}^{x_j}\left(\frac{\partial \widetilde{\varphi}_i}{\partial x}\right)^2 dx/\widetilde{U}_i \tag{3.19}$$

In the following the assumption is made that $2EI/t^2$ is constant over the length of the beam. In this way, equation (3.19) can be rearranged to give an indication of the change in rigidity of an element:

$$\frac{(E_{xx}Izz/t^2)_j}{(\widetilde{E_{xx}Izz}/t^2)_j} \equiv \frac{\widetilde{F}_{ij}}{F_{ij}} = \frac{\int_{x_{j-1}}^{x_j}\left(\frac{\partial \widetilde{\varphi}_i}{\partial x}\right)^2 dx/\int_0^l (\frac{\partial \widetilde{\varphi}_i}{\partial x})^2 dx}{\int_{x_{j-1}}^{x_j}(\frac{\partial \varphi_i}{\partial x})^2 dx/\int_0^l\left(\frac{\partial \varphi_i}{\partial x}\right)^2 dx} \tag{3.20}$$

Information of m more measured modes can be incorporated into the damaged index β for element j as indicated in the following equation:

$$\beta_j = \sum_{i=1}^{m}\widetilde{F}_{ij}/\sum_{i=1}^{m}F_{ij} \tag{3.21}$$

An advantage of this formulation is that the modes do not need to be normalized. A disadvantage can be that it is hard to determine a threshold value to indicate whether

damage is present or not. For a higher significance and to be able to make a better distinction between whether there is damage or not the damage index shown in equation (3.21) can be normalized. This is shown in equation (3.22).

$$Z_j = \frac{\beta_j - \mu}{\sigma} \tag{3.22}$$

In this equation μ represents the mean value of the damage indices and σ represents an estimation of the standard deviation of the damage indices.

3.3 Closing remarks

This chapter first stated the different levels of damage identification. Two modal analysis methods were described because these are needed in order to be able to apply the two SHM methods which were described thereafter. In the next chapter both modal analysis methods will be applied and the test setup will be described. Later the SHM methods will be applied to identify a known damage.

4 - Experimental Setup and pristine verification

The hardware and software components of the experimental setup will be described in this chapter . Subsequently, the pristine behavior of the composite blade is investigated. The mode shapes and eigenfrequencies will be determined with both the EMA and OMA technique in order to determine the effectiveness of the output-only method. Finally, the operational mode shapes and frequencies will be compared with the analytical properties determined in section 2.5.

4.1 Testing Setup

A schematic front view of the composite blade is shown in figure 4.1. The hatched area at the left side represents the clamped area. The piezo strain sensors will be placed in two rows of 16 measurement points. In this way, it should be possible to localize the damage over the length of the blade and the side of the blade the damage located.

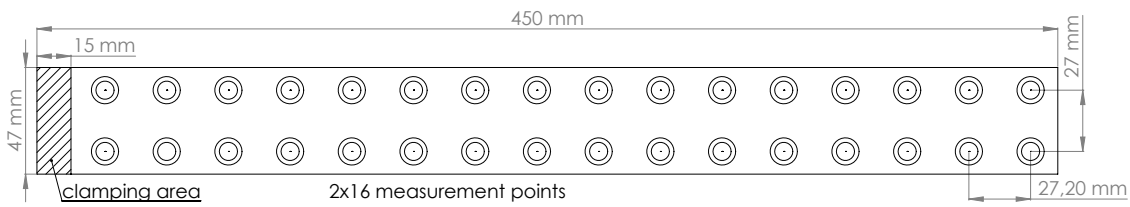

Figure 4.1: Front view of the composite blade to indicate the location of the measurement points and clamping area.

A schematic overview of the complete experimental setup with data acquisition hardware is shown in figure 4.2. As indicated earlier, piezo sensors are used to measure the strain on the surface in the length direction of the blade. The output of these piezo diaphragm is a voltage. As mentioned earlier, the advantages of these sensors are that they are very cheap and easy to mount on the blade. A disadvantage is, however, that the sensors are not calibrated. Due to this, the output of every sensor can differ and it can be hard to extract the mode shapes. However, since the methods used are based on differences between the pristine and damaged case it is not likely that this will be a problem.

Two boundary condition cases will be considered. In the first case the torsion spring,

indicated with number 3 in figure 4.2, will be removed and in the second case the spring will be kept in place. These two cases will be considered with the aim to see whether the boundary conditions of the system have a big influence on the damage detectability. In conclusion:

- Boundary condition case 1: Without torsion spring
- Boundary condition case 2: With torsion spring

The blade will be excited with a sine sweep by a shaker placed on the root of the blade. To be able to use the input force, and thus the EMA method, a force sensor is mounted between the root and the shaker. The data is managed using a NI-PXI platform equipped with an arbitrary waveform generator, embedded controller and two 8-channel dynamic signal acquisition modules. This means that each measurement one row of the piezo sensors can be measured. The sound and vibration measurement software developed by the University of Twente will be used to control the data. The frequency range will be from 20-1500 Hz. It is assumed that enough information is available in this range. As a result of the sampling frequency and zero padding the frequency resolution is 0.7813 Hz

4.2 Repeatability, experimental versus operational method

Every measurement is performed three times in succession and the mode shapes and corresponding frequencies are determined with both the experimental and operational method. It turned out that the first mode shape of the system was hard to find due to noise in the system. In order to keep the report organized, this chapter shows for every case and method only the second to fifth mode shape. In appendix A, all mode shapes found with the different methods are shown. Because the sensors used are not calibrated, the repeatability of the measurements is checked to determine whether strange peaks in the mode shapes occur due to this lack of calibration or due to some other cause. The modal assurance criterion (MAC) can be used to determine the consistency between two modal vectors. The MAC values range from zero, representing no consistency, to one, representing a consistent mode shape. In this manner, if two modal vectors have a strong correspondence the MAC value should approach unity. The MAC is defined as [20]:

$$MAC(m,n) = \frac{|(\psi_m^1)^T(\psi_n^2)^*|^2}{((\psi_m^1)^T(\psi_m^1)^*)((\psi_n^2)^T(\psi_n^2)^*)} \tag{4.1}$$

In this equation ψ_m^1 is the modal vector of mode m obtained at the first measurement and ψ_n^2 the modal vector of mode n obtain at the second measurement. The first four bending modes obtained are shown for boundary condition case 1 (without torsion spring) in figure 4.3 and for boundary condition case 2 (with torsion spring) in figure 4.4. In the figures the two sensor rows are plotted parallel to each other. The experimentally determined mode shapes are plotted in red and the operational mode shapes are plotted in black. Actually, three experimental and three operational are plotted. In this view the differences between the measurements of the same methods can however not be distinguished.

The corresponding frequencies are shown in table 4.1. The MAC values are obtained for both methods and each mode shape. The minimum MAC value of both the experimental and operational mode shapes for three measurements is 0.99. From this it can be concluded

that the measurements are highly repeatable and the strange peaks, like for example the peak of the first row of the first mode shape at $X = 250$, are due to the lack of calibration and will not give problems since the structural health methods are reference based.

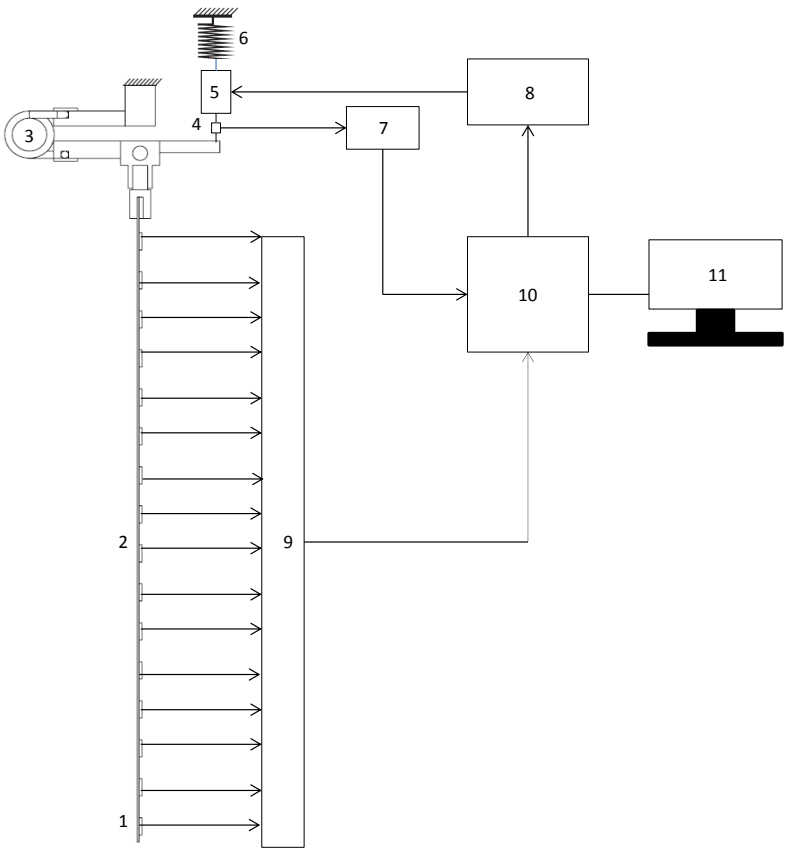

#	Description	Hardware	#	Description	Hardware
1	32 x Piezo diaphragm	Murata 7BB-12-9	7	Condition amplifier	B&K Nexus
2	Composite blade		8	Power amplifier	B&K 2706
3	Torsion spring	SF-VFR 8503	9	Conversion box	
4	Force transducer	B&K 8001	10	Data acquisition	NI-PXI
5	Shaker	B&K 4810	11	Sound and vibration	v3.0.20
6	Spring			measurement system	

Figure 4.2: Measurement setup and hardware for the experimental work.

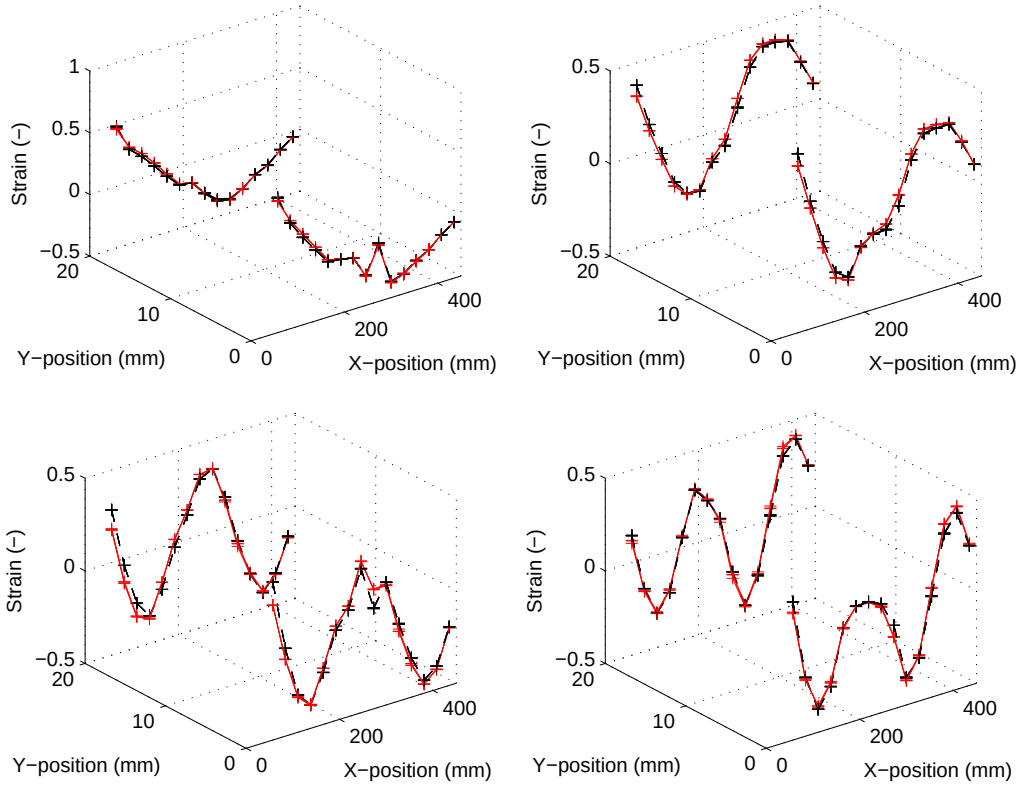

Figure 4.3: First four experimental (red) and operational (black) bending mode shapes, boundary condition case 1.

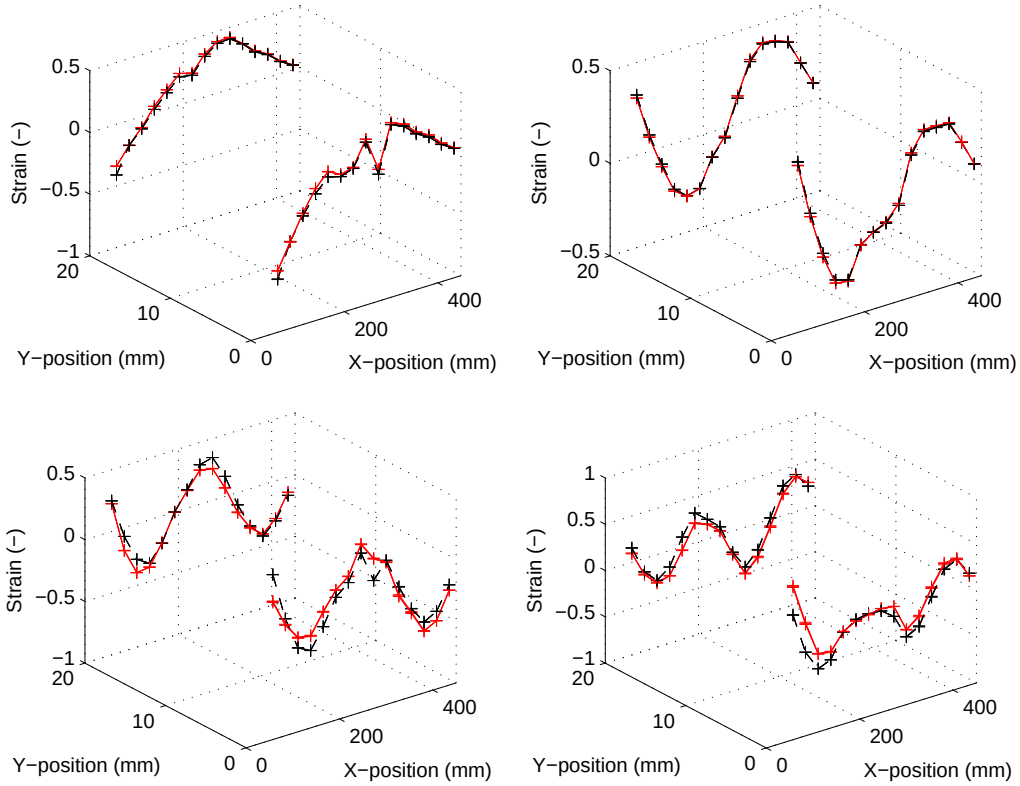

Figure 4.4: First four experimental (red) and operational(black) bending mode shapes, boundary condition case 2.

From table 4.1 it can be concluded that the frequencies for both methods are approximately the same. The maximum difference is 3 discrete frequency steps, 2.3439 Hz. Moreover, it cannot be said with confidence that this error originates from the operational method because it is sometimes hard to determine the exact position of the frequency peak in both methods, due to noise in the frequency response function. This is especially an important point in case two where more noise from the environment is present because of the torsion spring. To solve this problem, more advanced averaging and peak picking methods could be implemented in order to lower the noise level.

Table 4.1: Eigenfrequencies of the mode shapes shown in figure 4.3 and 4.4.

Mode number	**Case 1 OMA**	**Case 1 EMA**	**Case 2 OMA**	**Case 2 EMA**
1	35.15 Hz	36.72 Hz	30.47 Hz	29.69 Hz
2	90.62 Hz	90.62 Hz	86.72 Hz	85.94 Hz
3	169.53 Hz	170.31 Hz	166.41 Hz	165.63 Hz
4	276.56 Hz	278.91 Hz	276.56 Hz	274.22 Hz

The Modal assurance criterion can also be used to determine the performance of the operational modal analysis method with respect to the experimental modal analysis method. This is done because the EMA method is commonly used and straightforward to implement. If the results of both methods are comparable, it can be concluded that the output-only method can be used for damage assessment. The MAC values comparing the OMA and EMA method are shown in table 4.2. It can be seen that the shapes of case 1 are matching very good. The values of case 2 are somewhat lower. This can also be seen in figure 4.4. The origin of this can again be found in the higher noise level. It can be concluded that the confidence in the output-only method is sufficient to use this method for damage detection.

Table 4.2: MAC values between OMA and EMA method.

Mode number	**Case 1**	**Case 2**
1	0.99	0.99
2	0.99	0.99
3	0.97	0.91
4	0.99	0.82

4.3 Analytical versus operational method

In the last part of this chapter, the analytically determined mode shapes derived in section 2.5 and shown in figure 2.4 will be compared with the operational mode shapes of boundary condition case 1 and 2. This is done for two reasons. The first reason is to check whether every analytically determined mode shape can actually be measured. The second reason is to determine the behavior of the demonstrator. The analytical derivation showed the extreme hinged and clamped cases. These figures can be used to see which behavior the demonstrator is showing. In figure 4.5 the first four operational mode shapes are plotted

together with the analytical mode shapes with approximately the same behavior. Only one of the sensor rows is plotted. This is done to obtain a more clear plot and because the behavior of the two rows is approximately the same. All mode shapes found are again shown in appendix A. It can be seen that both cases show almost the same behavior. Some points are more deviating than other points. For example, the seventh sensor from the left side in the first and fourth mode shape has a relatively large error with respect to the analytical mode shape. It is assumed that this error originates from the lack of calibration of the sensors. This assumption is confirmed by the fact that this sensor is a bit off in the other mode shapes. It turns out that the behavior of both operational cases approaches the clamped analytical mode shapes. A reason for this can be that the friction in the hinge is relatively high compared with the stiffness of the blade, which is relatively low. Like stated before, due to noise the first analytical mode shape was not clearly detected with the operational method.

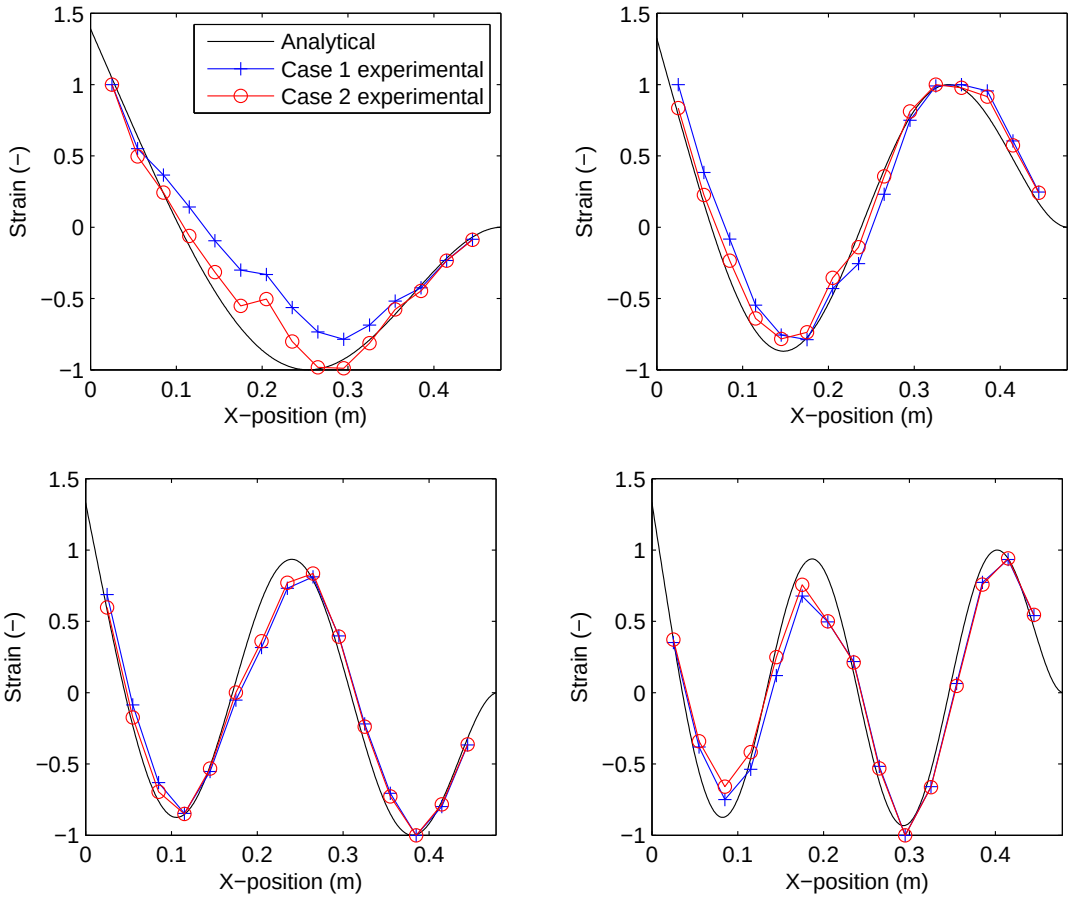

Figure 4.5: Analytical versus Operational mode shapes.

The natural frequencies were also checked for both cases. It turns out that the added mass of the piezo sensors cannot be neglected in order to get matching frequencies. The piezo sensors add 4.6 gram to the blade, which is about 10 % of the total mass. The analytical frequencies with added mass are shown in table 4.3. The corresponding operational and experimental frequencies were already shown in table 4.1. It can be seen that, with

the added mass, the results are matching relatively good. For boundary condition case 1 the maximum difference in frequency is 5.95 Hz and for boundary condition case 2 4.64 Hz.

Table 4.3: Analytical natural frequencies of the mode shapes shown in figure 4.5.

Mode number	**Analytical natural frequencies**
1	30.77 Hz
2	86.18 Hz
3	168.04 Hz
4	278.86 Hz

5 - Experimental test results

This chapter will show the results of the application of the SHM methods to determine damage, as described in chapter 3. First, the damage scenarios will be described. Thereafter, it is tried to determine the location and severity of a single damage on the blade. Finally, the possibility to detect multiple damages is investigated. All measurements in this chapter are carried out with the operational modal analysis technique.

5.1 Damage scenarios

The structural integrity of a composite blade can be assessed with on-blade monitoring. Damage progression of composite materials is often very local, like stated earlier. Therefore, damage is only applied to one or more small areas of the blade. Damage progression results in mechanical degradation of the blade. This can be indicated as a local reduction of bending stiffness.

Damage scenarios will be simulated by increasing the mass of the blade locally with point masses, instead of reducing the bending stiffness. Both increasing the mass and reducing the bending stiffness should approximately have the same influence on the blade. However, by adding mass the blade is not actually damaged. This means that more damage scenarios can be investigated with the same blade and measurements can be repeated if necessary. Oosterik [2] indicates that the local reduction of bending stiffness of a composite blade subjected to delamination is between 10 and 20 %. Assuming that adding mass and reducing the bending stiffness have the same impact on the dynamic properties of the blade, the mass addition should also be in this order of magnitude.

Different damage scenarios are considered. Parameters that could be changed are the location of the damage, the severity of the damage, and the number of damage locations. All damage scenarios will be considered for both boundary condition cases. The considered damage scenarios are shown in table 5.1. The damage severities low, medium and high respresent mass additions of respectively 6, 13, and 20 %.

To clarify table 5.1, figure 5.1 shows a schematic overview of the different damage locations and severities. The table can be divided into two sections. The upper section describes the damage scenarios consisting of a single damage at different locations for both boundary condition cases and variable severity. The lower section describes the more advanced damage scenarios consisting of two damage locations. Masses mounted on location 1 and 2 of figure 5.1 will be considered for both boundary condition cases with increasing and equal damage severity of both locations and with deviating damage severity between the two points. In the following sections, the same distinction is made. First, the SHM methods will be applied on the cases with one added mass. Thereafter, the

two added mass cases will be considered. This distinction is made because in this way the most effective method can be used for the two mass cases. Furthermore, it is assumed that it will be easier to identify one damage location and harder to determine two locations of damage.

Table 5.1: Considered damage scenarios. The upper section contains the single damage cases. Each subcase consists of 3 measurements with severities increasing from low to high. The lower section consists of the multiple damage cases. Subcase 4 contains the equal severity cases, also with severities increasing from low to high. Subcase 5 contains unequal damage severities for point 1 and 2.

Damage scenario #		**boundary condition**	**X-location**	**Y-location**	**Severity**
1.1	L/M/H	1	x_1	y_1	L/M/H
1.2	L/M/H	1	x_2	y_2	L/M/H
1.3	L/M/H	1	x_3	y_3	L/M/H
2.1	L/M/H	2	x_1	y_1	L/M/H
2.2	L/M/H	2	x_2	y_2	L/M/H
2.3	L/M/H	2	x_3	y_3	L/M/H
1.4	L/M/H	1	x_1, x_2	y_1, y_2	LL/MM/HH
2.4	L/M/H	2	x_1, x_2	y_1, y_2	LL/MM/HH
1.5	HL	1	x_1, x_2	y_1, y_2	H,L
1.5	LH	1	x_1, x_2	y_1, y_2	L,H
2.5	HL	2	x_1, x_2	y_1, y_2	H,L
2.5	LH	2	x_1, x_2	y_1, y_2	L,H

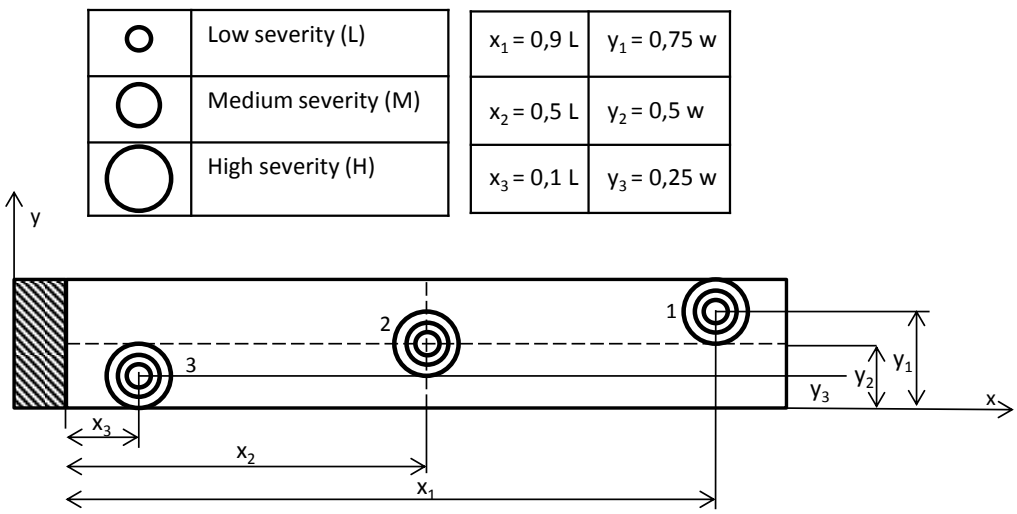

Figure 5.1: Schematic overview of the damage locations and severities.

5.2 Results single damage location

The damage scenarios of the upper section of table 5.1 are performed. For each case, a reference and damaged measurement is carried out. To determine the consistency between the reference and damage mode shapes, the MAC-values are again calculated. Figure 5.2 shows the MAC-values of the matching modes of the first eight mode shapes of the single damage cases considered in this section. It can be seen that the minimum MAC-value of the scenarios of boundary condition case 1 is 0.7 and of case 2 is 0.58. Thus, it can be concluded that the mode shapes are clearly affected by the damage, but there is still a reasonable correspondence.

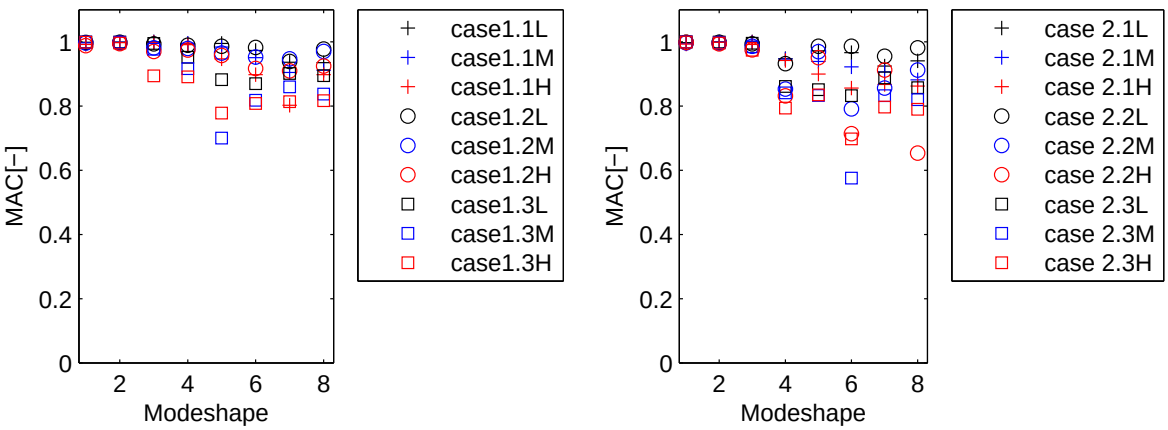

Figure 5.2: Modal Assurance criterion case 1 (left) and case 2 (right).

5.2.1 Modal curvature damage index

The theory of the MC-DI is explained in section 3.2.1. This section will determine how effective the method is in identifying the applied damages. The aim is to obtain a robust SHM system that can identify every single damage of the same boundary condition case. The MC-DI can be calculated for each mode shape. To be able to implement this method in a monitoring system the same mode shapes should give a positive result for all three damage scenarios of the same boundary condition case.

Figure 5.3 shows the second mode shape of the scenarios of the first boundary condition case. The approximate location of the actual damage is given with an arrow. This mode shape is shown because scenario 1.1 and 1.3 show the best result for this scenario. The first eight mode shape curvatures for every case are shown in appendix B. It can be seen that the location where the mass is mounted shows a peak and the peak value is increasing for accumulating damage severity. Scenario 1.1 and 1.3 are also showing relatively large peaks at other places. These peaks are however always smaller than the peaks at the damage location. Problems arise when the damage at the middle of the blade is assessed. The second figure gives no indication that a damage is present at location two. It turns out, none of the mode shapes of this scenario is able to identify this damage. Figure 5.4 shows the results of boundary condition case two. The actual damage is again indicated with an arrow. For scenario 2.1 and 2.3 again the second mode shape shows the best results. It

can be seen that the damages can be located relatively good. The second damage location is again not detected. Other mode shapes do not show better results.

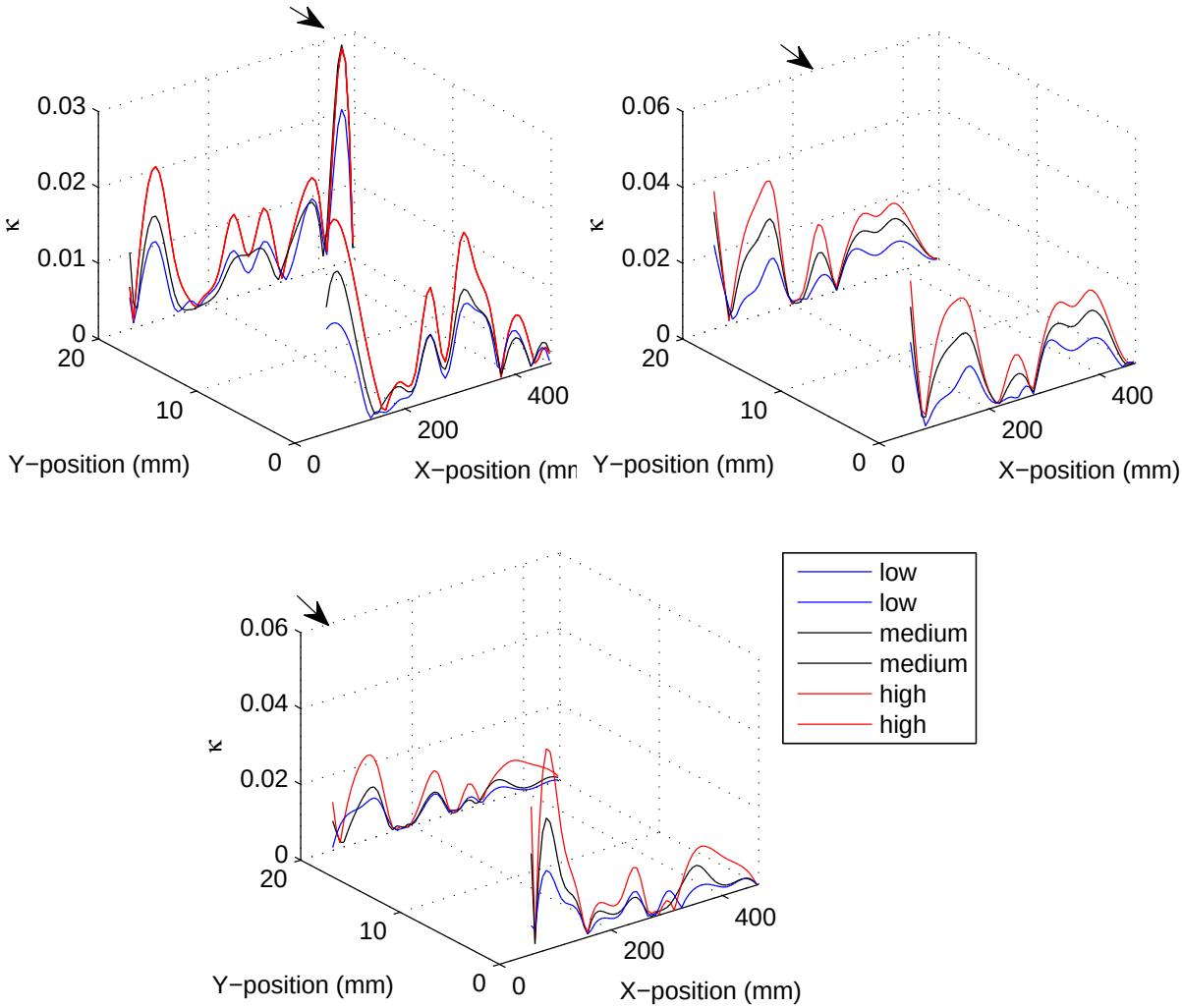

Figure 5.3: Modal curvature damage index of case 1.1, 1.2 and 1.3. Mode shape 2. Black arrow gives damage location.

The reason for the poor performance of the second location with respect to the other locations can possibly be explained by the following reasons. The first location is close to the tip of the blade. At this location the amplitude of the vibrations are the largest. For this reasons, although the curvature is small, the sensitivity for damage can be larger. The third location is close to the clamped area. From the pristine mode shapes shown in appendix A it can be seen that the curvature in the largest in this area. Therefore, the sensitivity in this area can also be large. Damage at the second location can be hard to find because most mode shapes show nodes close to the location of the damage. Therefore, the curvature is often small in the area of the damage and the sensitivity can be lower.

From the results obtained with the MC-DI it can be concluded that this method cannot be used to detect and localize different damage locations with confidence. The

shown figures indicate that the methods can be used to detect, localize and determine the severity of damage at some locations. The second location can however never be detected. The method will not be used further in this thesis to try to identify the more advanced cases because it is already shown that the performance is not sufficient.

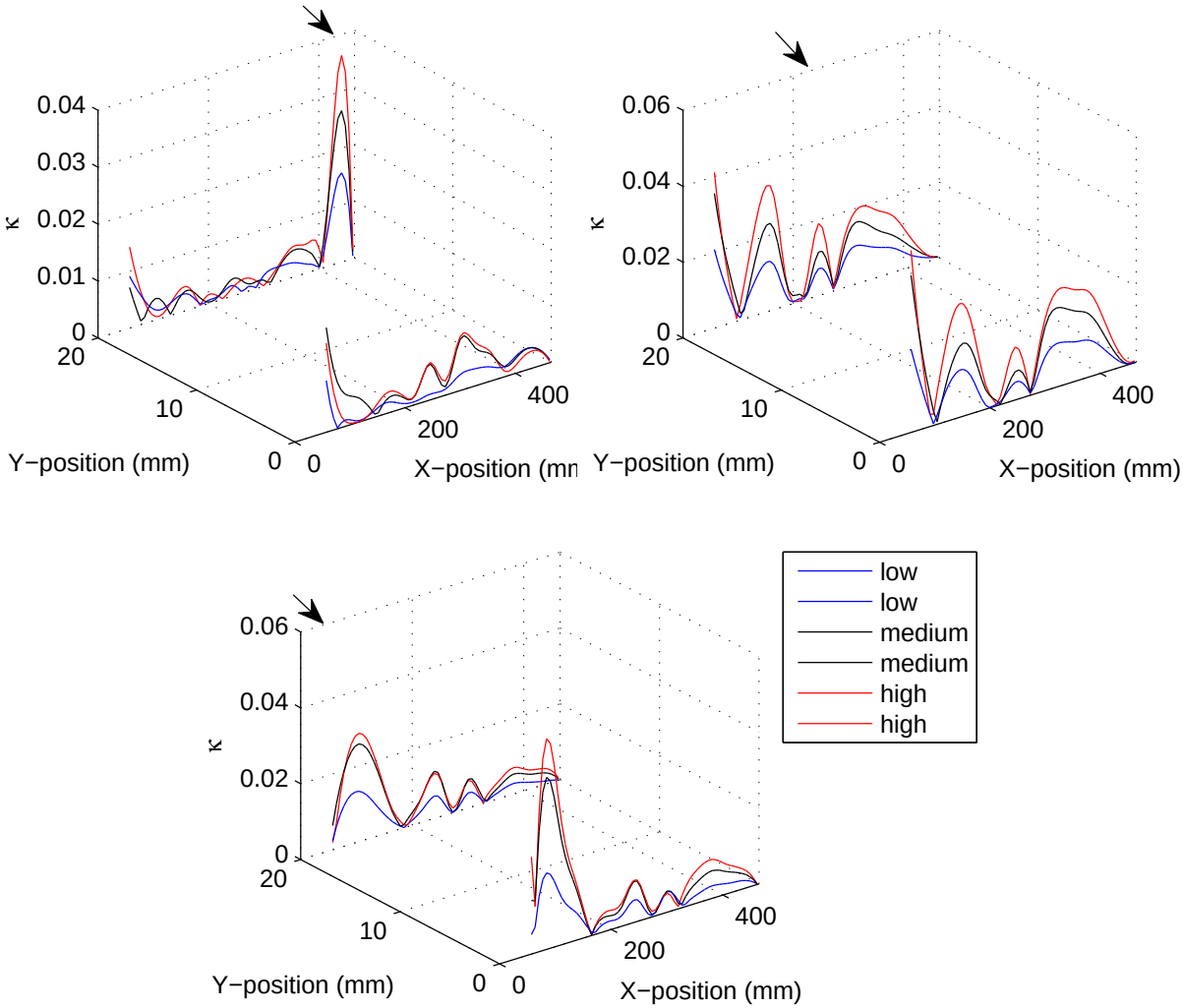

Figure 5.4: Modal curvature damage index of case 2.1, 2.2 and 2.3. Mode shape 2. Black arrow gives damage location.

It should be noted that it is also possible to sum the damage index of more modes like explained with the MSE-DI. This is also investigated, but gave no additional insights. Therefore, the results are not shown in this section.

5.2.2 Modal strain energy damage index

The theory of the MSE-DI is explained in section 3.2.2. As indicated earlier, a range of mode shapes can be used to calculate the damage index. Figure 5.2 confirmed that the first eight modes can be obtained. The results in this section are given for the first five

modes. This is done because in this way the best results were obtained for every damage scenario. This can be explained by the increasing complexity of the higher mode shapes. This increasing complexity can introduce errors between the reference and damaged case which are not originating from the added mass. Another explanation can be that the peaks of higher modes are lower and, therefore, harder to find. This can also be the cause of the poor results with taking higher modes. Figure 5.5 shows a 3D and top view of an example case to make clear how the results will be shown. At the left side an isometric view is shown. Every bar indicates a calculated damage index value. Because this view is not easy to read and not all bars can be seen the top view will be used in the rest of this section. In this way, a lot of information can be shown using small space. The actual damage location is indicated with an arrow. Appendix C shows the 3D view of all MSE figures shown in this chapter.

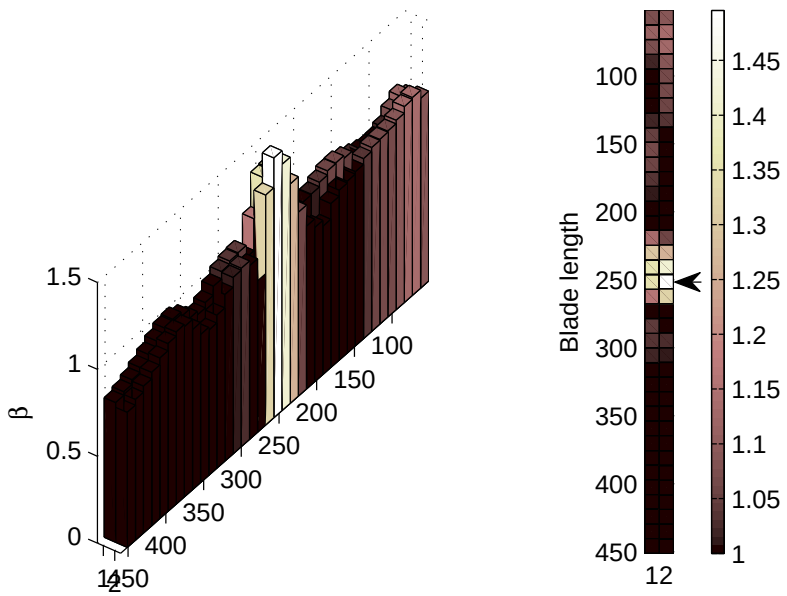

Figure 5.5: MSEDI, Case 1.2 C in 3D and top view.

For reasons discussed later, the β damage index from equation (3.21) will be shown in the following results instead of the normalized index. When no damage is present this index should be one. Damage locations should give a peak. Figure 5.6 shows the scenarios of both boundary condition cases at location one, for accumulating severity. The results are scaled to the maximum peak value of the high severity scenario. This is done because this scenarios contains most likely the highest peak. It can be seen that the method is able to locate the added mass on the end of the blade for both boundary condition cases. The results for case 1 show, however, a lot less false positive peaks than case 2. Furthermore, the highest peak value is indicated at the wrong side of the blade. The inferior results of case 2, already predicted in chapter 4, comes from the higher level of noise. Finally, both scenarios indicate clearly that the severity of damage is increasing.

Figure 5.7 shows the scenarios of both boundary condition cases at location two, for accumulating severity. It can be seen that the peak values of this scenarios are a lot lower than the previous cases. Furthermore, there is a lot more noise present in these cases.

Contrary to the MC-DI, this method is able to locate the damage for boundary condition case 1. Also, a clear increasing severity can be seen. The performance of case 2 is again less convincing. The damage is located at approximately the right location and the severity is also increasing indicated by the maximum peak value. The results of case 1 are, however, a lot better.

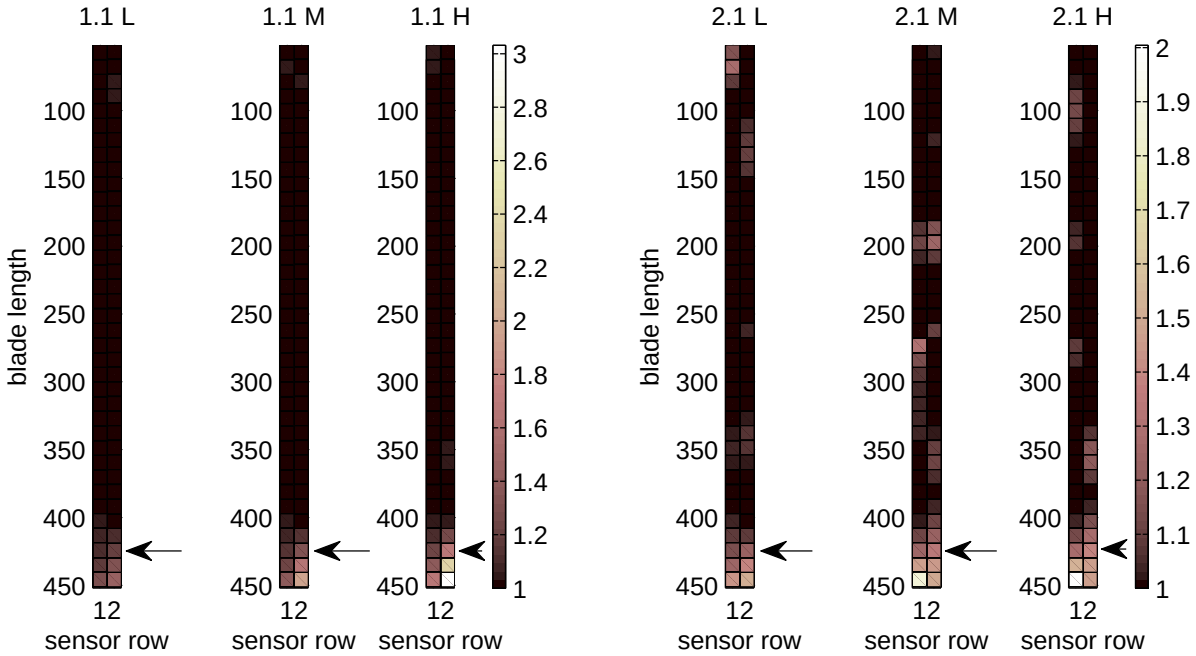

Figure 5.6: MSEDI of location 1, with increasing damage severity, of both cases.

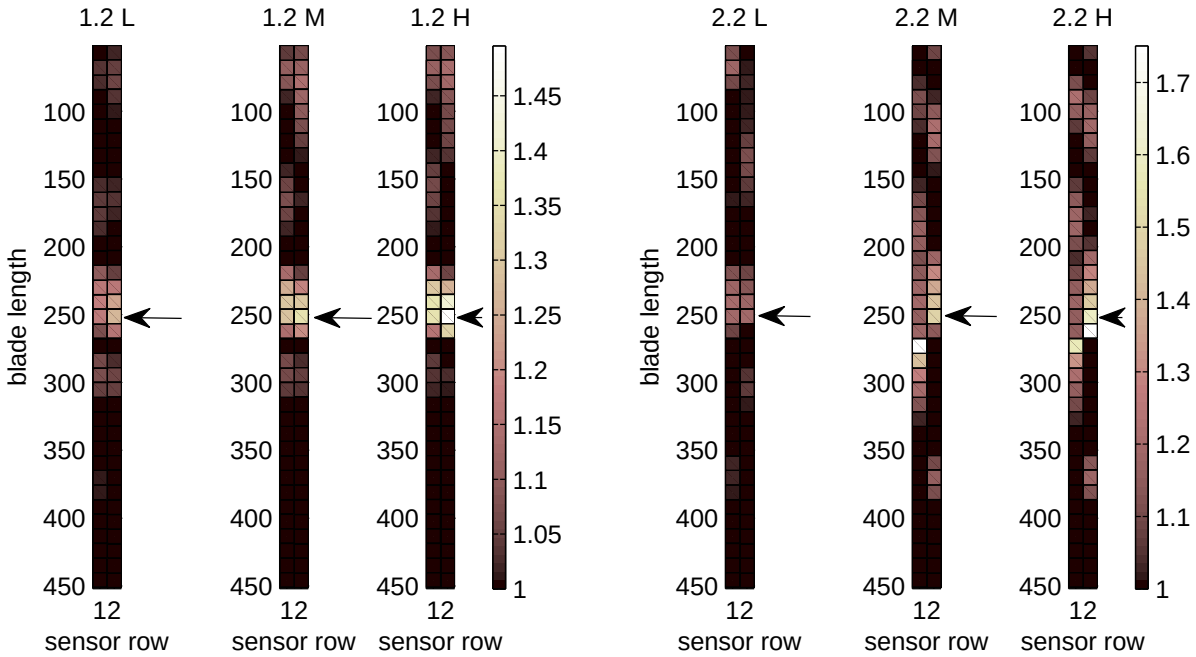

Figure 5.7: MSEDI of scenario 2, with increasing damage severity, of both cases.

Finally, the results of location three are shown in the same way as the previous cases in figure 5.8. It can be seen that that added mass is located at the right location for both boundary condition scenarios. Furthermore, there are some false positive peaks in both cases but none of them come closer than about 50 mm to the actual damage location. In both cases it is possible to see the effect of the increasing damage severity.

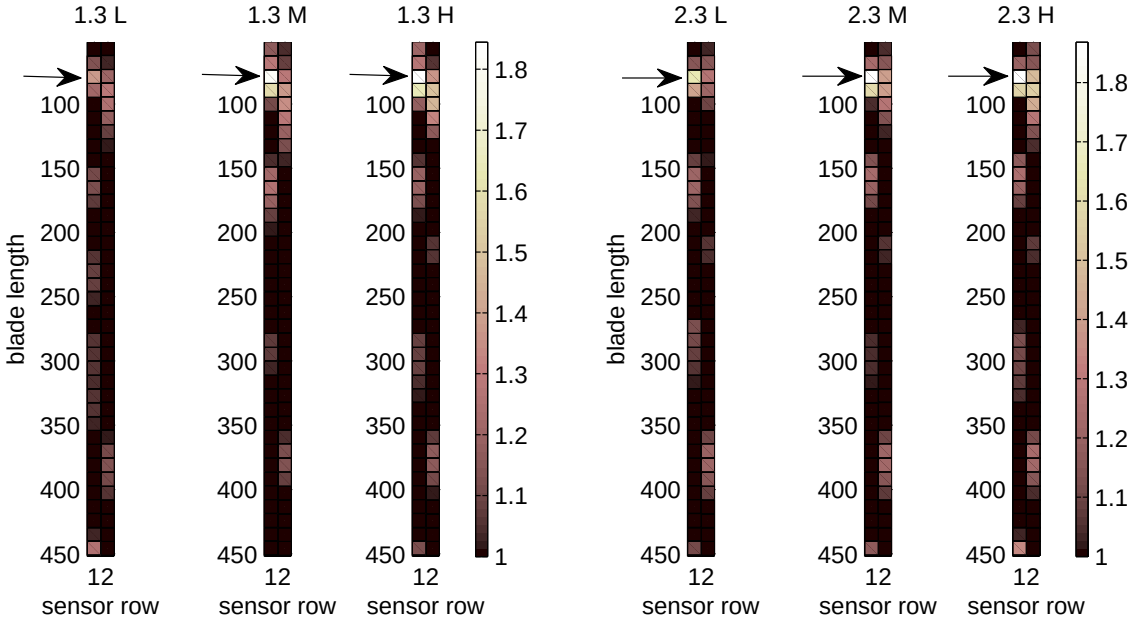

Figure 5.8: MSEDI of scenario 3, with increasing damage severity, of both cases.

As discussed earlier, detecting the damage at the middle of the blade is very difficult. This can also be seen by looking at the maximum peak values, which are the lowest at this location. In the previous part of this section it was discussed that the MSE-DI is able to locate the damage relatively good. Also the increasing severity was observed in all cases. However, to design a robust SHM system a threshold peak value should be stated to trigger that there actually is a damage present. Figure 5.9 shows the peak values of the previously shown scenarios for both the normal and normalized damage index.

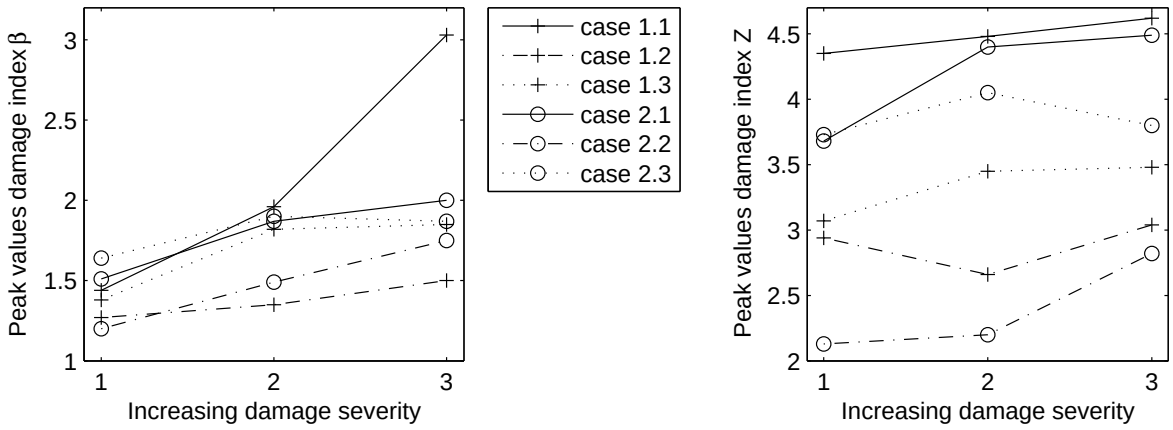

Figure 5.9: Peak values with both damage index definitions. On the horizontal axis: 1=L, 2=M and 3=H.

From the figure it can be concluded that the β value is increasing for every scenario while this is not the case for the normalized Z values. This can be explained by the fact that the damage index is normalized by the mean value and standard deviation of the damage index. When the damage index is increasing, the mean value and standard deviation can also increase. Due to the fact that the behavior of these parameters is not known, the severity indication of the Z value is also not known. The threshold value of the damage index is dependent on the peak values and the value of the first false positive peak. The highest false positive peak of boundary condition case 1 is 1.28. As can be seen on the left side of figure 5.9, only the peak damage index value of case 1.2L is lower than this values. This means that the threshold value to detect damage in boundary condition case 1 should be at least 1.28. Damages starting from medium severity can than be detected. case 2 is showing a lot more noise at every scenario. The highest false positive value is however only 1.34. As can again be seen in figure 5.9, only case 2.2L cannot be detected. The threshold value for this boundary condition case should at least be 1.34. All damages from medium severity can then be detected.

5.3 Results 2 damage locations

In this section, the MSE-DI will be applied to the more advanced damage cases from table 5.1. Masses will be added to location 1 and 2 of figure 5.1. This is done because this is the worst case scenario. The previous section made clear that identifying damage at location 2 is hard, but most times possible. Therefore, it is interesting to see whether it is also possible to identify damages at these two locations, instead of location 1 and 3. In scenario 1.4, equal damages are mounted. Scenario 5 uses the same damage locations. This time one of the locations will have high severity while the other location has low severity damage. Only the MSE-DI will be applied. This is done because, in contrast with the MC-DI, this method gave promising results for the single damage cases.

Modal strain energy damage index

Figure 5.10 shows the results of damage scenario 4 for both boundary condition cases and accumulating damage severity. As could be expected from the results from the previous chapter, it is very hard to localize the damage at location two at the middle of the blade. This could be predicted because of the low peak value at this location with respect to the peaks at damage location one. It can be seen that both peaks from scenario 1.4 are bigger than the false positive peaks at other location. However, the peaks are not getting higher for accumulating damage. Therefore, it is not possible to assess the damage severity.

For scenario 2.4 it is also possible to detect the two damage locations. Furthermore, there is also some indication that the damage is increasing. the biggest problem with this case is, however, the peaks at the clamped side of the blade. These peaks are in the same order of magnitude as the actual damage. Therefore, it is not possible to determine a threshold value for damage.

The scenarios with deviating damage severities are shown in figure 5.11. scenario 1.5 HL and 2.5 HL have high severity at location one and low severity at location two. As could be expected, the damage at location two cannot be identified at all. For boundary condition case 1 a small peak can be seen. This peak has however the same magnitude as multiple other peaks on the blade. For boundary condition case 2 the other peaks on

the blade are even bigger. Scenario 1.5 LH and 2.5 LH have low severity at location one and high severity at location two. AS could be expected, the peaks at location two are more clear in these scenarios, while the damage at location one could still be obtained very clearly. For boundary condition case 1, both locations are now easy to detect and other peaks are a lot lower. For boundary condition case 2 both peaks are also present. Other false positive peaks are, however, also present in the same order of magnitude. Therefore, it is again hard to indicate which of the peaks the real damage location is.

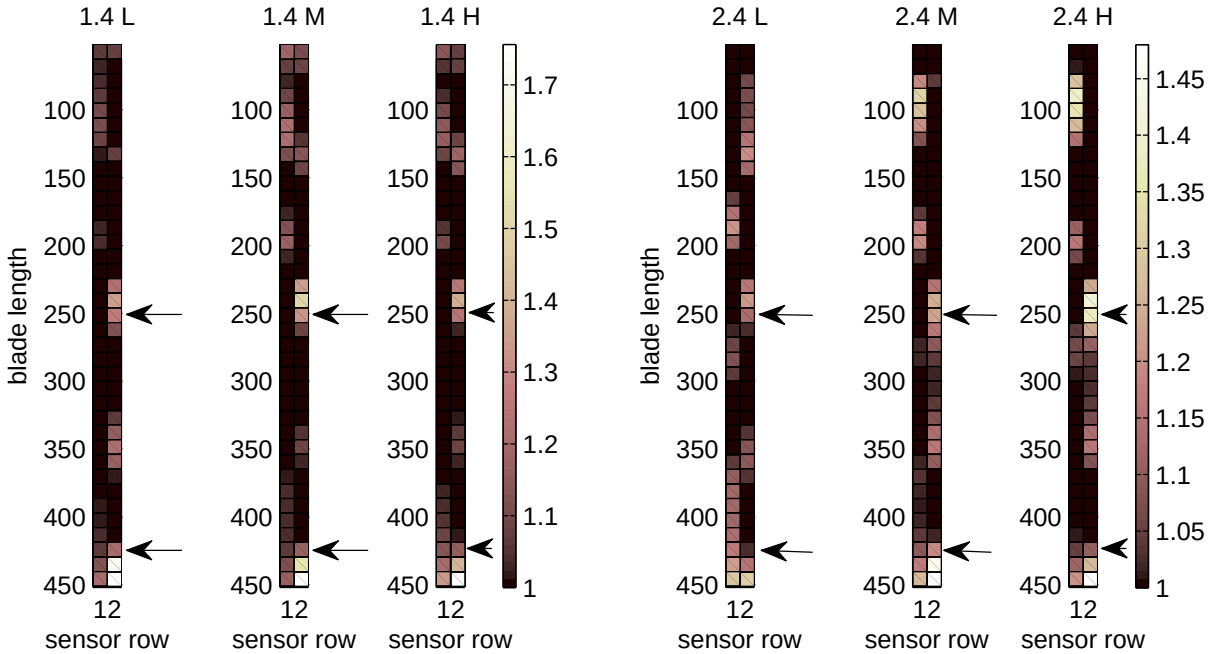

Figure 5.10: MSEDI of scenario 4, with increasing damage severity, of both cases.

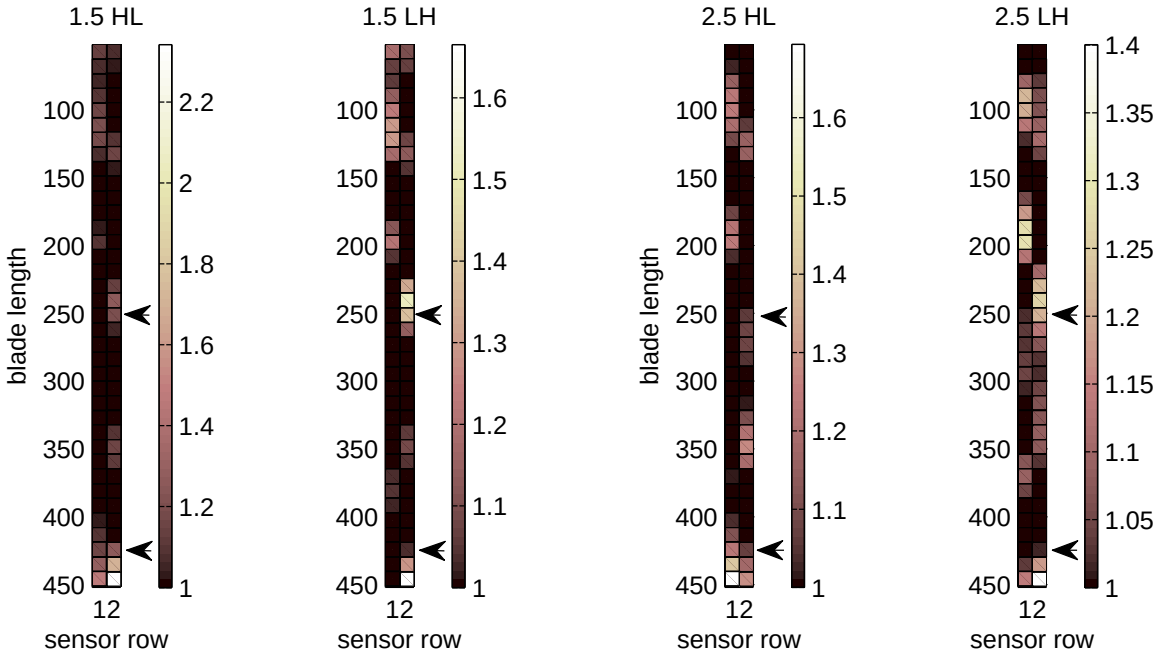

Figure 5.11: MSEDI of scenario 5,with unequal damage severity, of both cases.

5.4 Closing remarks

The current chapter first discussed how damage was applied on the blade and at what locations. Next, the results of the single damage location cases were discussed. It was concluded that the MSE-DI is performing best and that most damages can be identified with confidence. Finally, the more advanced two damage cases were discussed. In most cases it was not possible to identify all the damages. The next chapter will state the conclusions by answering the research questions.

6 - Conclusions & Recommendations

This report described the application of SHM techniques on a composite blade with realistic helicopter boundary conditions. The experimental work was performed using a in-house developed demonstrator. Furthermore, the possibility to use only output vibrations is investigated. Below, the research questions will be answered. Subsequently, recommendations for further research will be discussed.

6.1 Conclusions

First, the sub questions will be answered. These answers will be used to answer the research question.

- *Can a properly working test setup with reduced complexity be obtained?*

A properly working, flapping blade, experimental setup is obtained. The pristine behavior of the experimental setup is described in chapter 4. Two different boundary condition cases were introduced. Both show approximately the same dynamic behavior. It can, however, be seen that the amount of external vibrations plays a big role in the damage detectability of the experimental setup.

- *Are operational modal analysis techniques suitable to detect damage in the test setup?*

In chapter 4, the pristine behavior of the experimental setup is determined with both the experimental and operational modal analysis technique. The consistency between these two methods was calculated with the modal assurance criterion. It can be concluded that the results are consistent and, therefore, that the operational technique can be used to implement the SHM methods.

- *Is there a distinction in the detectability of different composite damage scenarios?*

The results of both SHM methods for a range of damage scenarios and two different boundary conditions are shown in chapter 5. It turned out that the MC-DI was not performing like expected. The results from the MSE-DI were much better. When one mass was added to the blade it was possible to detect a medium severity damage at different locations on the blade and for both boundary condition scenarios. Also, all single location damages could be localized within a reasonable distance, about 30 mm, and a indication of the severity could be obtained. It should be noted that the results from boundary condition case 2 showed a lot more noise and were harder to interpret.

In the multiple damage scenarios it is much harder to determine the damage locations. With equal damages, it is only possible to identify the damage location for boundary condition case 1. The higher noise level makes that the peaks are not high enough in case 2. For unequal damage severity only one out of the four considered scenarios showed good results.

- *To what extend can damage in a composite beam structure subjected to rotor blade system boundary conditions be detected with modal-based techniques while only using output data ?*

Finally, the research question can be answered. Output only modal-based techniques are successful implemented on a composite blade experimental setup. The behavior of the setup is a step towards an actual rotor blade system. It can be concluded that a robust SHM system can be developed while the damages are concentrated on one location. It turns out to be very difficult to draw any conclusions on the health of the blade when multiple damage locations are present.

6.2 Recommendations

The current thesis leaves room for more research. As stated above, the results with one added mass were satisfying. However, the implementation of a robust SHM system for multiple damage locations was not possible. It could be investigated if other methods are more suitable for this job or whether the current method could be optimized for this aim.

Another recommendation is about the currently limited complexity of the experimental setup. This research focused on redesigning a current demonstrator in order to make it robust and properly working. There are a lot of possibilities to adjust the demonstrator more towards the real helicopter rotor blade system. The following things could be adjusted:

- Increase active degrees of freedom
- Increase blade complexity
- More realistic loading spectrum
- More realistic damage scenarios

More active degrees of freedom can be obtained by implementing the feathering and lagging hinge again in the demonstrator. With this adjustment the rotor blade system is fully articulated. New hinges should be designed because the old demonstrator was not functioning as expected. Furthermore, flapping will still be the most important motion of the blade.

In the current demonstrator a simple composite blade with constant and square cross-section over the length of the blade is used. A more realistic blade will consist of multiple different parts and more complex bending behavior. Moreover, multiple surfaces will be present which also will make implementing SHM a lot harder.

The experiments in this thesis are carried out with a sine sweep as input signal. Actual helicopter vibrations will probably have some frequency ranges which will be more excited

than others. This can give problems with the output only method which is derived for signal where every frequency is equally excited.

Finally, also the damage scenarios can be made more realistic. Currently, masses are added which gives a lot of possible damage scenarios and great repeatability possibilities. When actual damages will be assessed, more blades and more sensors should be available. This means more effort has to be put into the equipment. It would, however, be very nice to assess real impact damages or delaminated composite beams.

Bibliography

[1] T. Ooijevaar. Vibration based structural health monitoring of composite skin stiffener structures. Phd Thesis. University of Twente, 2013.

[2] S.E. Oosterik. Towards on-blade monitoring of rotor blade systems, a dynamic approach. Master Thesis. University of Twente, 2014.

[3] J. Wolters. Design and construction of a setup that represents the behavior of a helicopter rotor blade system. Master Thesis. University of Twente, 2014.

[4] A.R.S. Bramwell, George Done and David Balmford. Bramwell's Helicopter Dynamics. Butterworth-Heinemann, Second edition, 2001.

[5] Federal Aviation Administration. Helicopter Flying Handbook. U.S. Department of Transportation, 2012.

[6] L. Warnet and R. Akkerman. Composite Course lecture notes. University of Twente, 2011-2012.

[7] http://www.torayca.com/en/ visited 4-2-2014

[8] R.F. Gibson Principles of composite material mechanics Department of mechanical engineering. Wayne State University, Detroit, Michigan 1994

[9] http://composites.nl/documents/TCAC_MD_Cetex_properties.pdf Visited on 4-2-2015

[10] M. Meirovitch, Fundamentals of Vibrations, Singapore: McGrqw-Hill higher Education, 2001.

[11] A. Rytter. Vibration based inspection of Civil Engineering Structures, Aalborg: Dept. of Building Technology and Structural Engineering, Aalborg University. (Fracture and Dynamics; No. 44, Vol. R9314). 1993

[12] F.B.A. Schiphorst. Vibration based structural health monitoring Master Thesis University of Twente 2012

[13] P.D. Welch. The use of the Fast Fourier Transform for the estimation of powerspectra, IEEE transactions on audio and elcctro-acoustics, Vols. AU-15, no.2, 1967

[14] P. Cornwell, S.W. Doebling and C.R. Farrar Aplication of the strain energy damage detection method to plate-like structures. Journal of sound and vibration(1999) 224(2), 359-374

[15] B.J. Schwarz and M.H. Richardson Experimental modal analysis CSI Reliability week, orlando, FL, October, 1999

[16] H.Tijdeman and A de Boer Introduction to Modal Analysis and Experimental Vibration Measurement Lecture notes, University of Twente 2005

[17] R. Brinkcer, L. Zhang and P. Andersen Modal identification from ambient responses using Frequency Domain Decomposition Aalborg University 2000

[18] V.B. Dawari and G.R. Vesmawala Structural damage identification using modal curvature differences IOSR Journal of Mechanical and Civil engineering

[19] N. Stubbs, J. Kim and C. Farrar Field verification of a nondestructive damage localization and severity estimation algorithm

[20] R.J. Allemang, The modal assurance criterion, twenty years of use and abuse. University of Cincinnati,Cincinnati, Ohio 2003

Appendices

A - Pristine behavior demonstrator

In this appendix, the first eight found mode shapes and eigenfrequencies are shown in addition to the information shown in chapter 4. The red crosses are the measured values. Cubic splines are fitted to make the data more readable. Figure A.1 shows the mode shapes of case 1 determined with the experimental method. Figure A.2 shows the mode shapes of case 1 determined with the operational method. Figure A.3 shows the mode shapes of case 2 determined with the experimental method. Figure A.4 shows the mode shapes of case 2 determined with the operational method. Finally, figure A.5 shows the comparison of the analytically determined mode shapes versus the operational mode shapes of both cases.

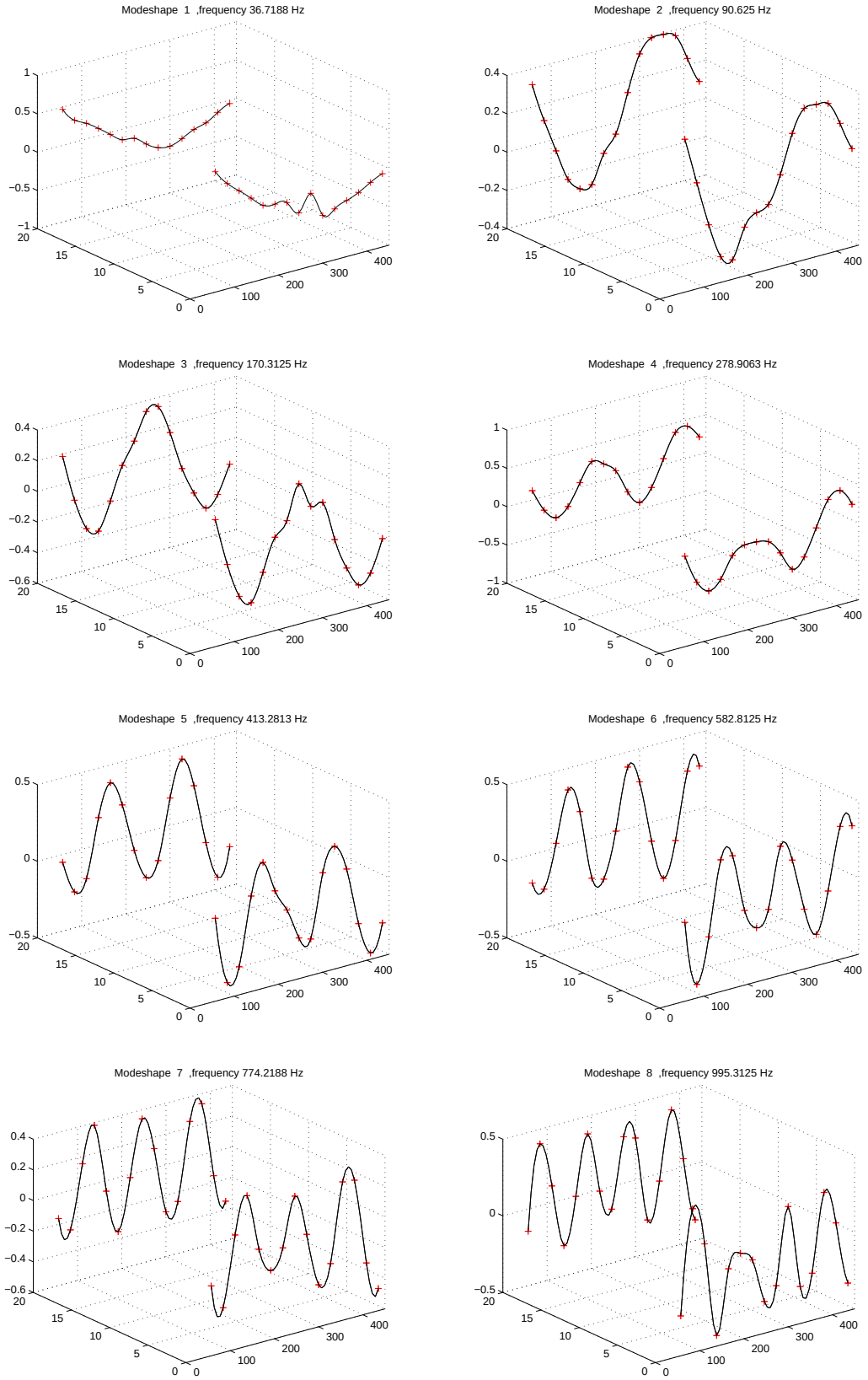

Figure A.1: EMA Case 1 mode shapes.

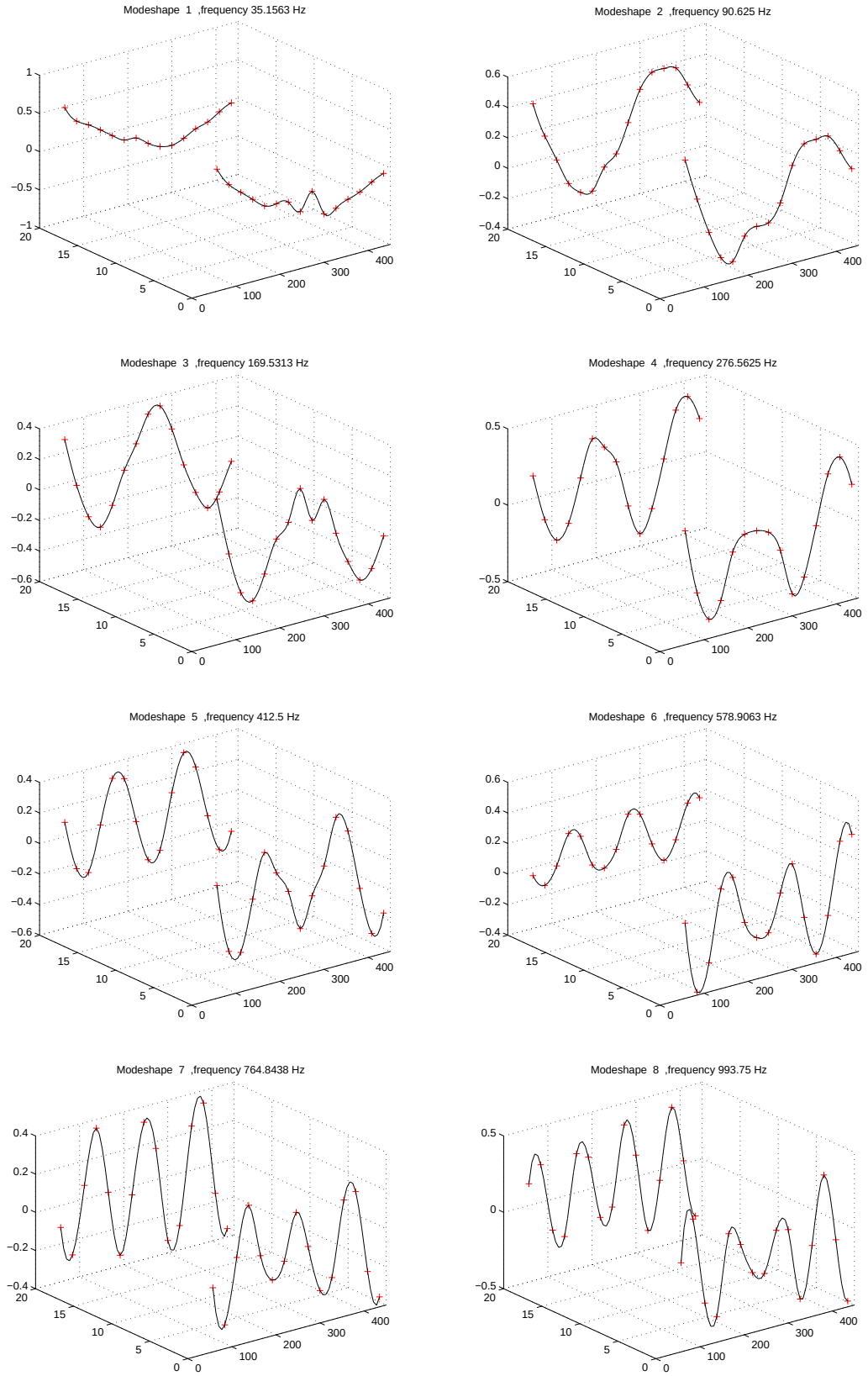

Figure A.2: OMA Case 1 mode shapes.

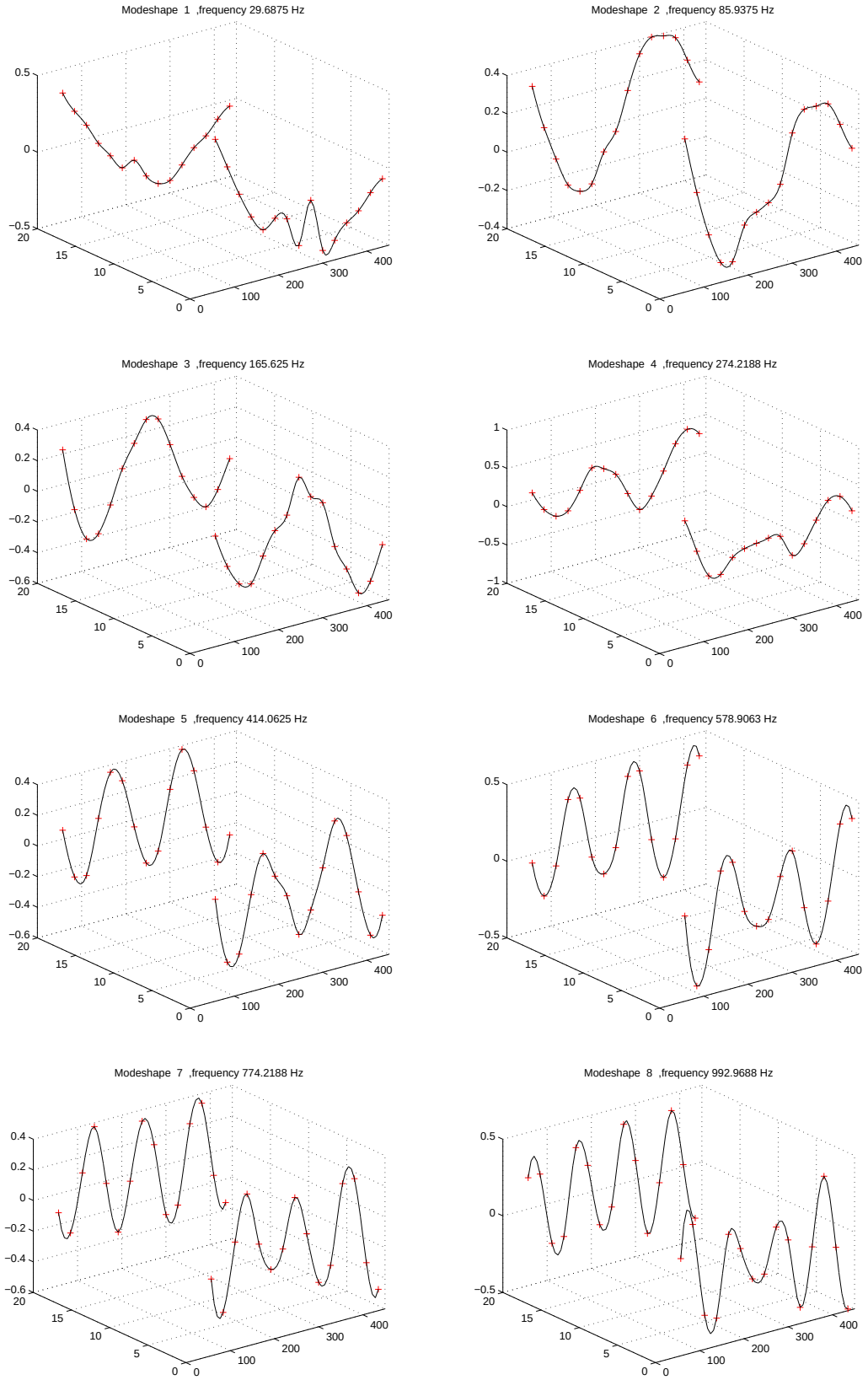

Figure A.3: EMA Case 2 mode shapes.

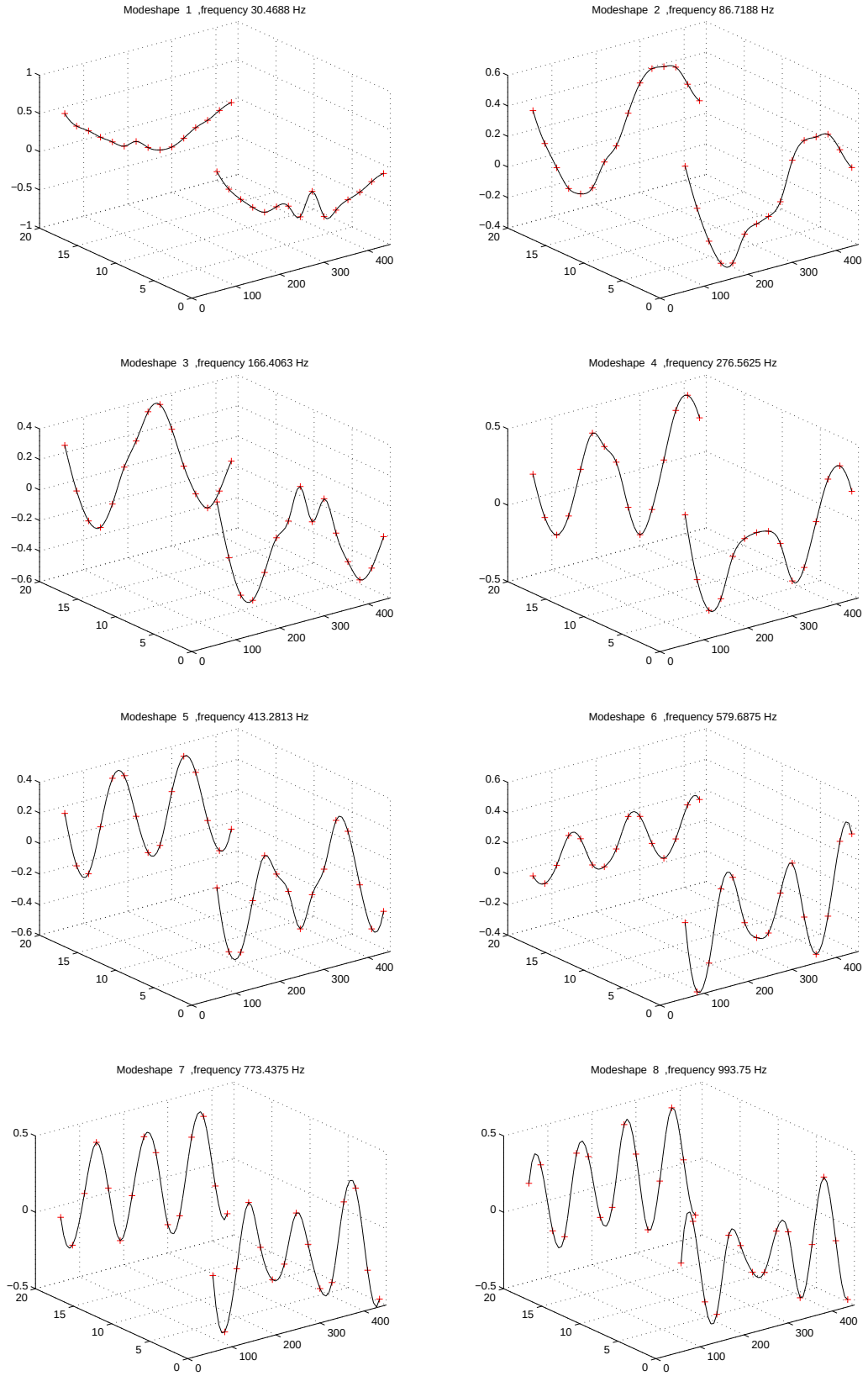

Figure A.4: OMA Case 2 mode shapes.

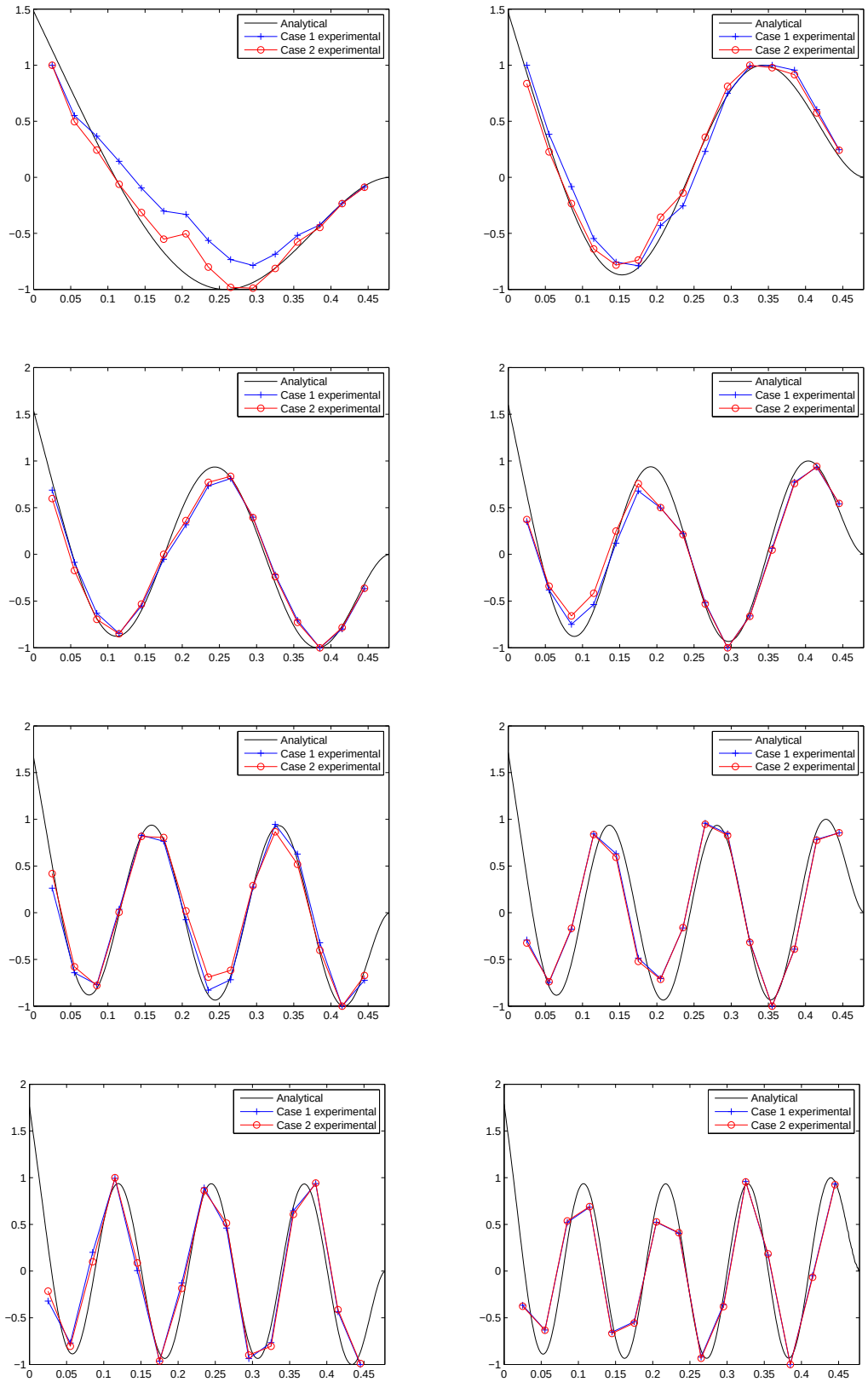

Figure A.5: Case 1 and 2 operational versus analytical mode shapes.

B - Modal curvature damage index figures

In this appendix, the MC-DI figures of the first eight mode shapes are shown. In chapter 5, only the second mode shape curvature damage is shown because this gave the best results. First, all figures of boundary condition case 1 will be given. Thereafter, the figures of boundary condition case 2 will be given. In every figure the blue line indicates the low severity case, the black one medium severity, and the red line indicates high severity damage.

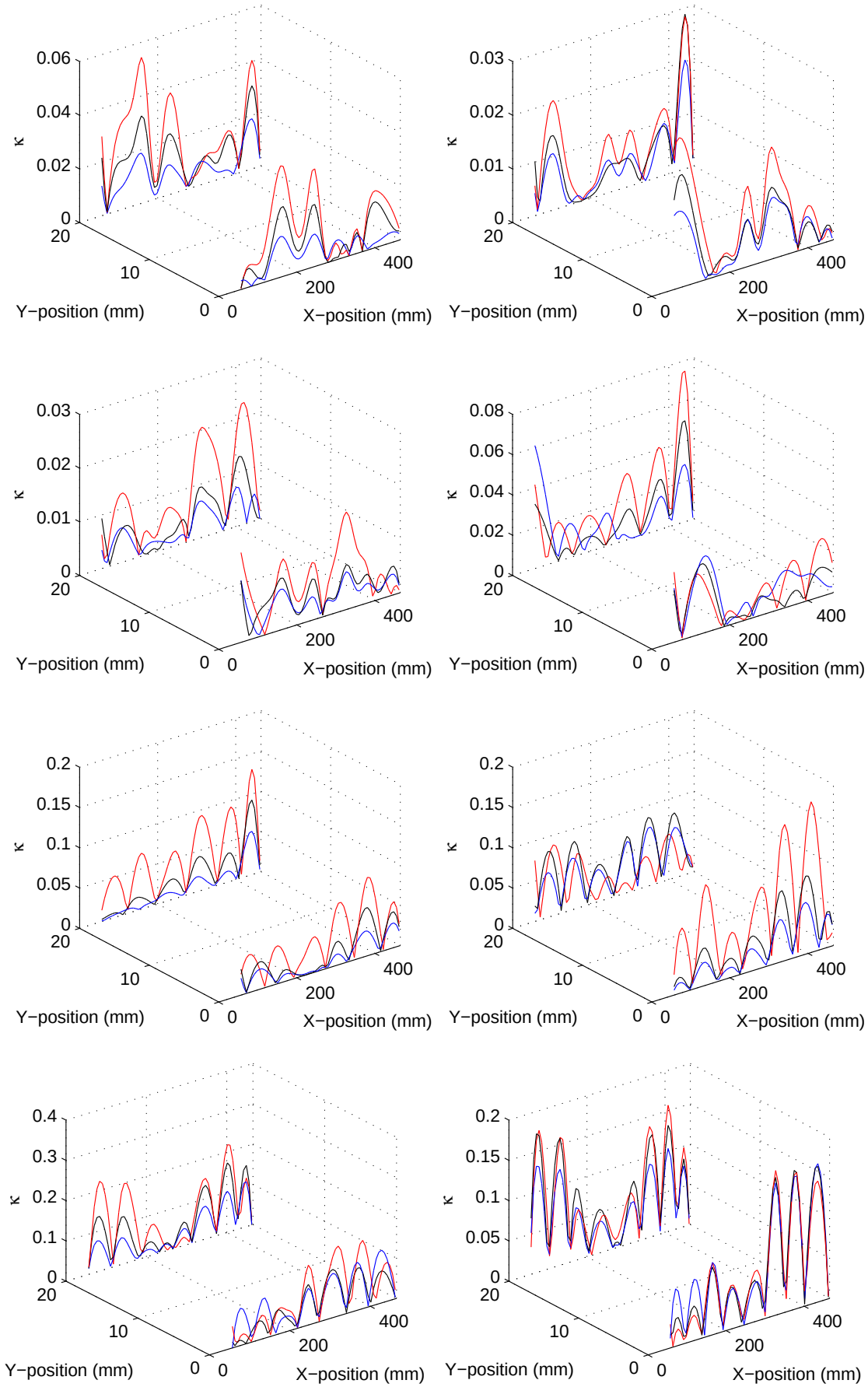

Figure B.1: Modal curvature damage index of the first 8 modes of case 1.1.

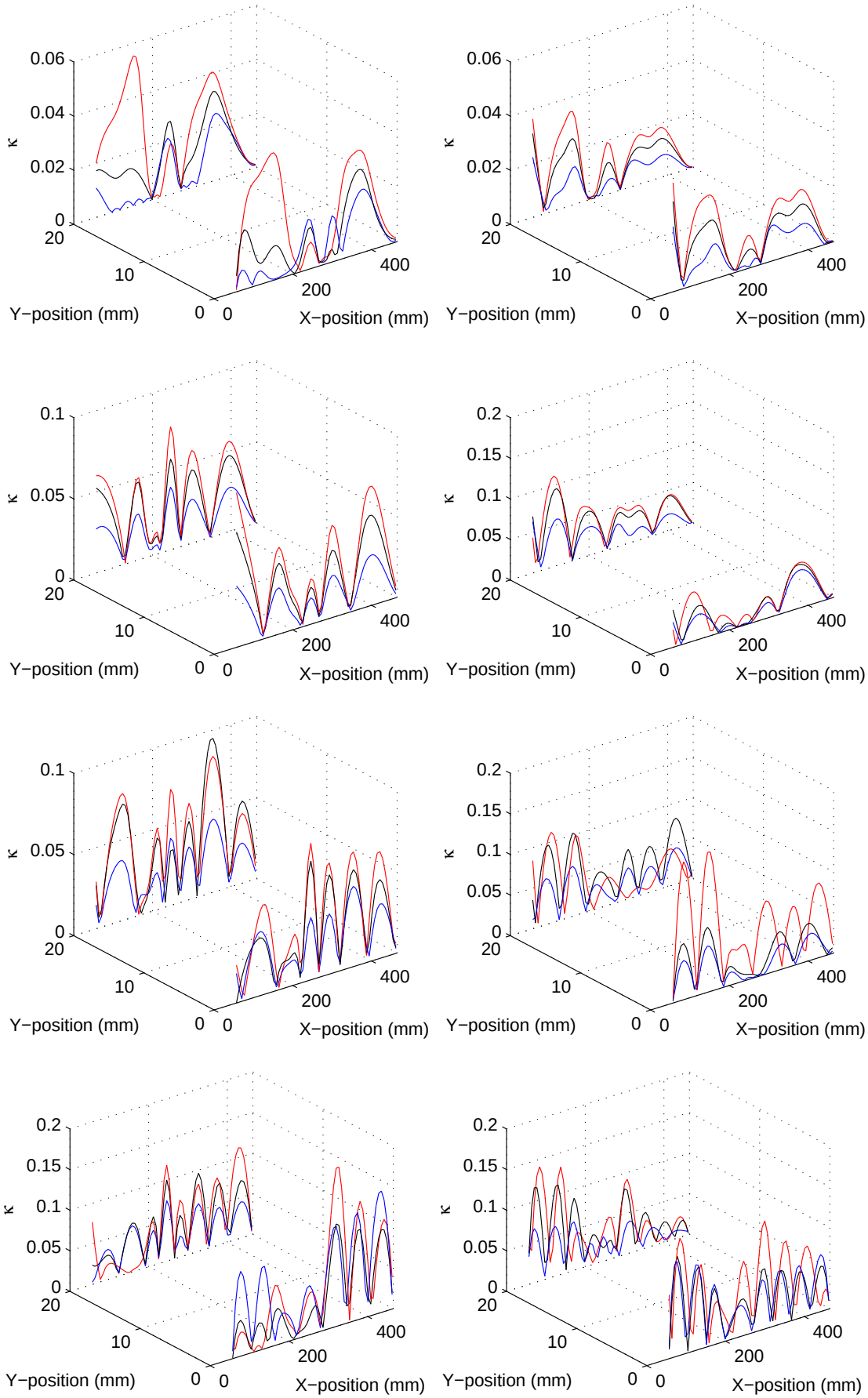

Figure B.2: Modal curvature damage index of the first 8 modes of case 1.2.

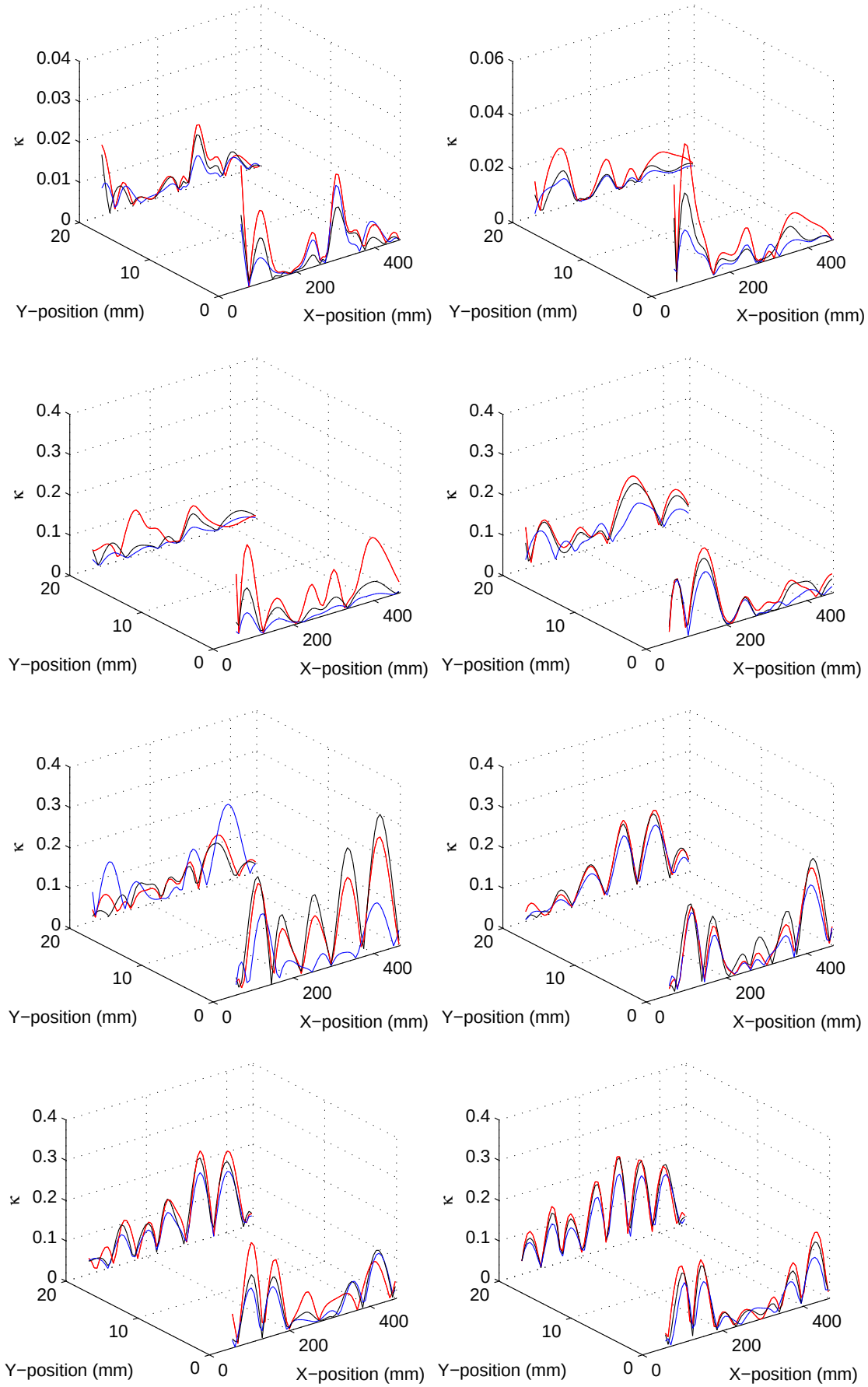

Figure B.3: Modal curvature damage index of the first 8 modes of case 1.3.

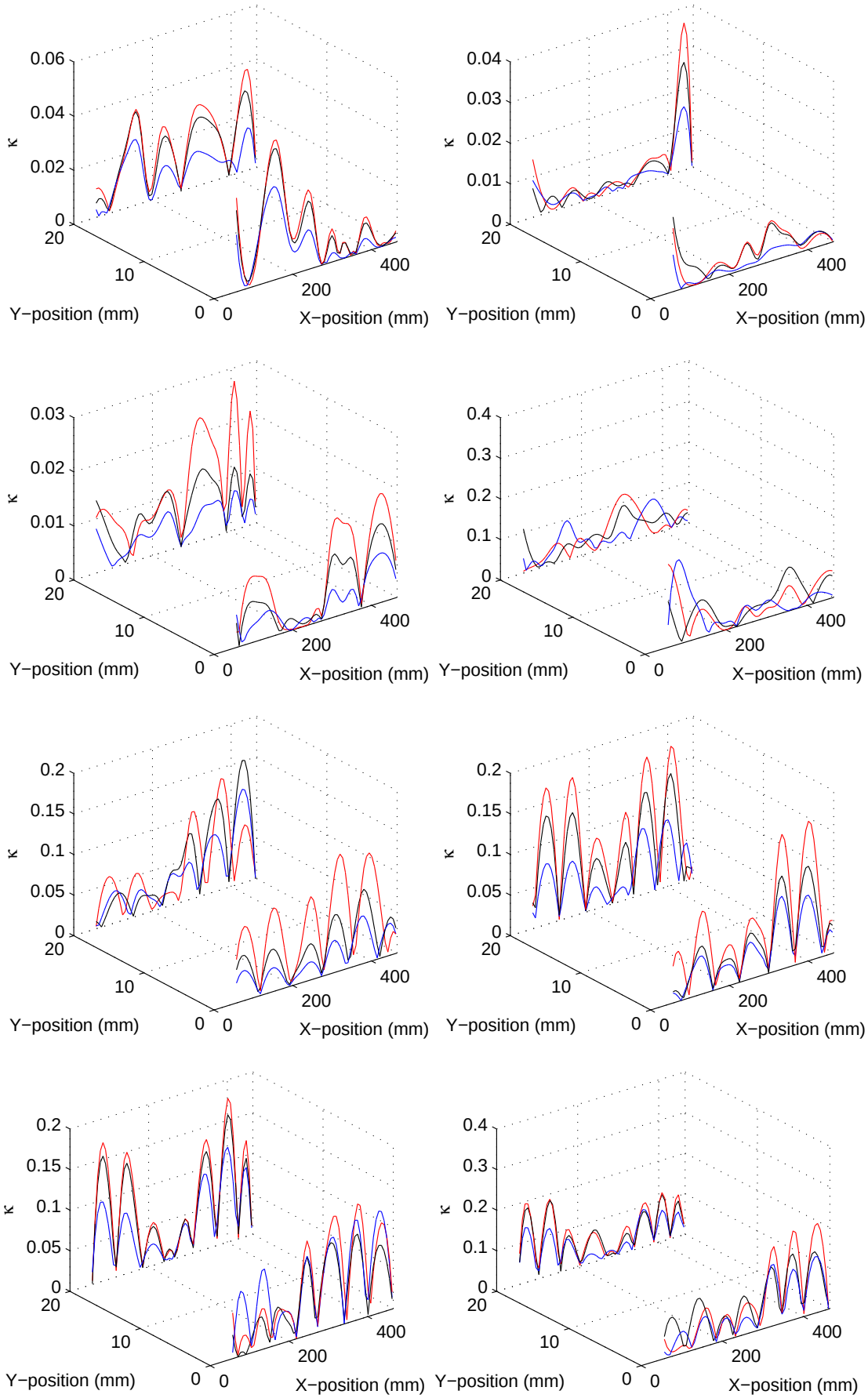

Figure B.4: Modal curvature damage index of the first 8 modes of case 2.1.

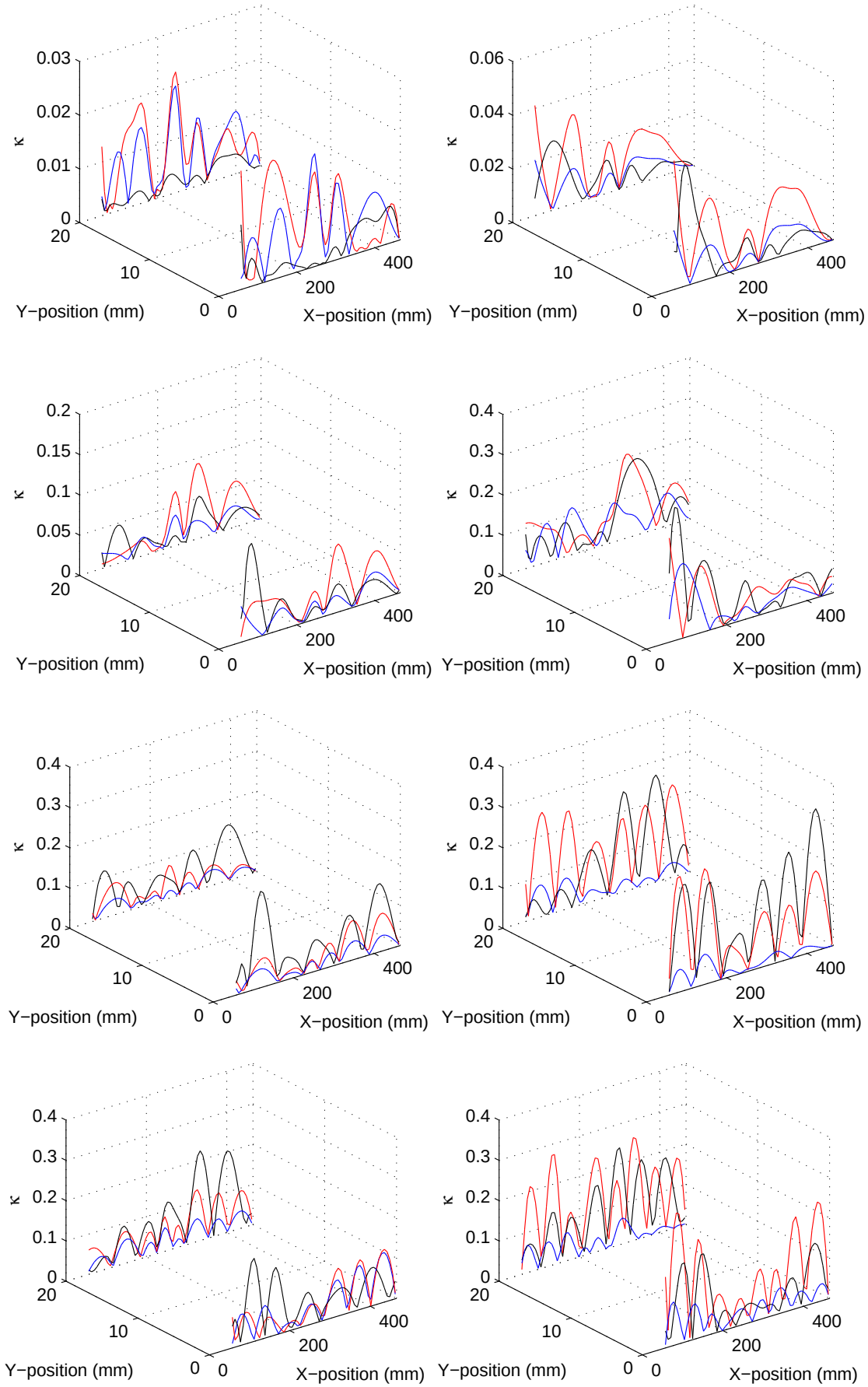

Figure B.5: Modal curvature damage index of the first 8 modes of case 2.2.

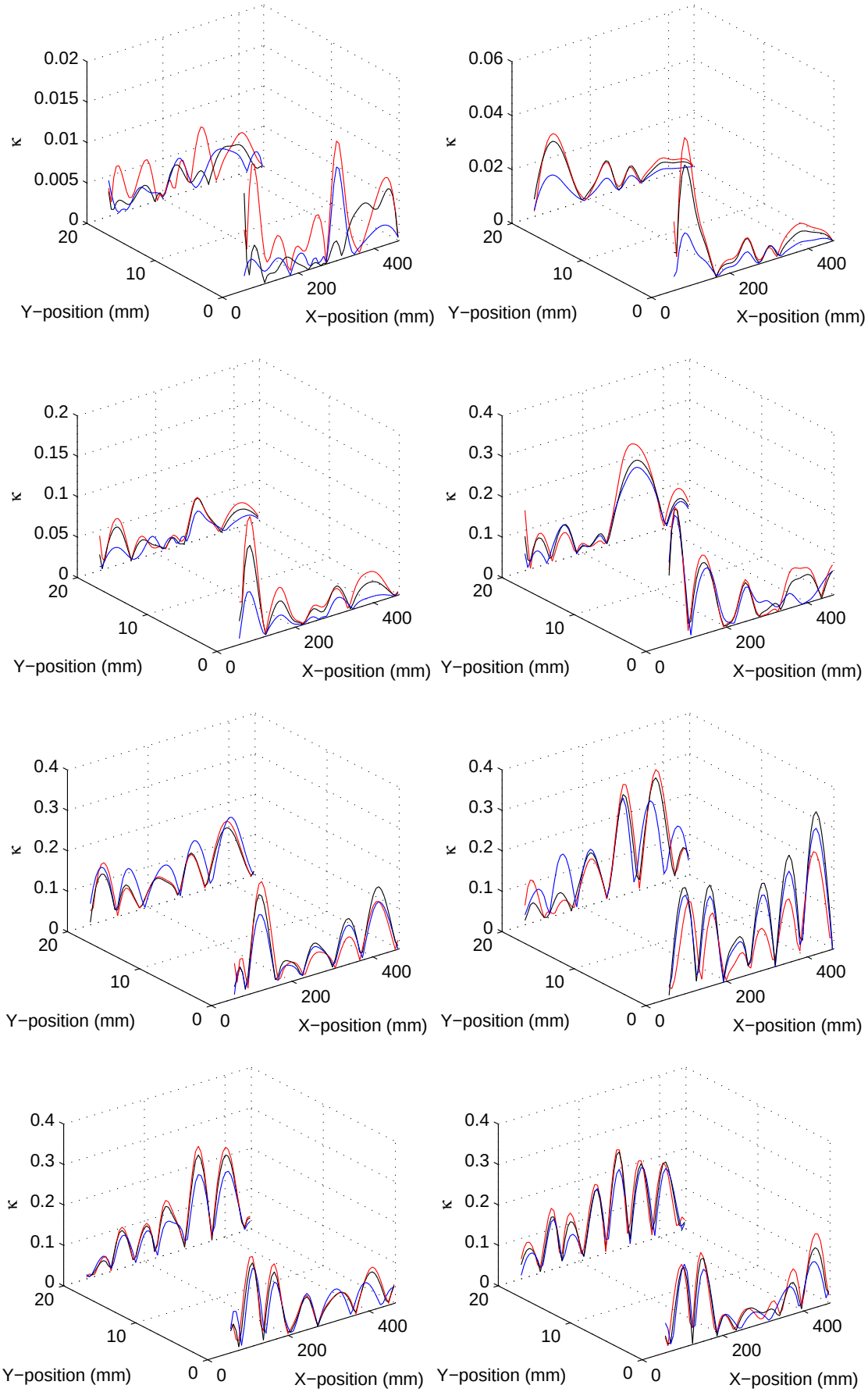

Figure B.6: Modal curvature damage index of the first 8 modes of case 2.3.

C - Modal strain energy damage index 3D figures

In this appendix, all MSE-DI figures are shown in 3D and top view. For clarity, only the top view was shown in chapter 5. All figures are scaled to the maximum peak value. First, all figures of boundary condition case 1 will be given. Thereafter, the figures of boundary condition case 2 will be given.

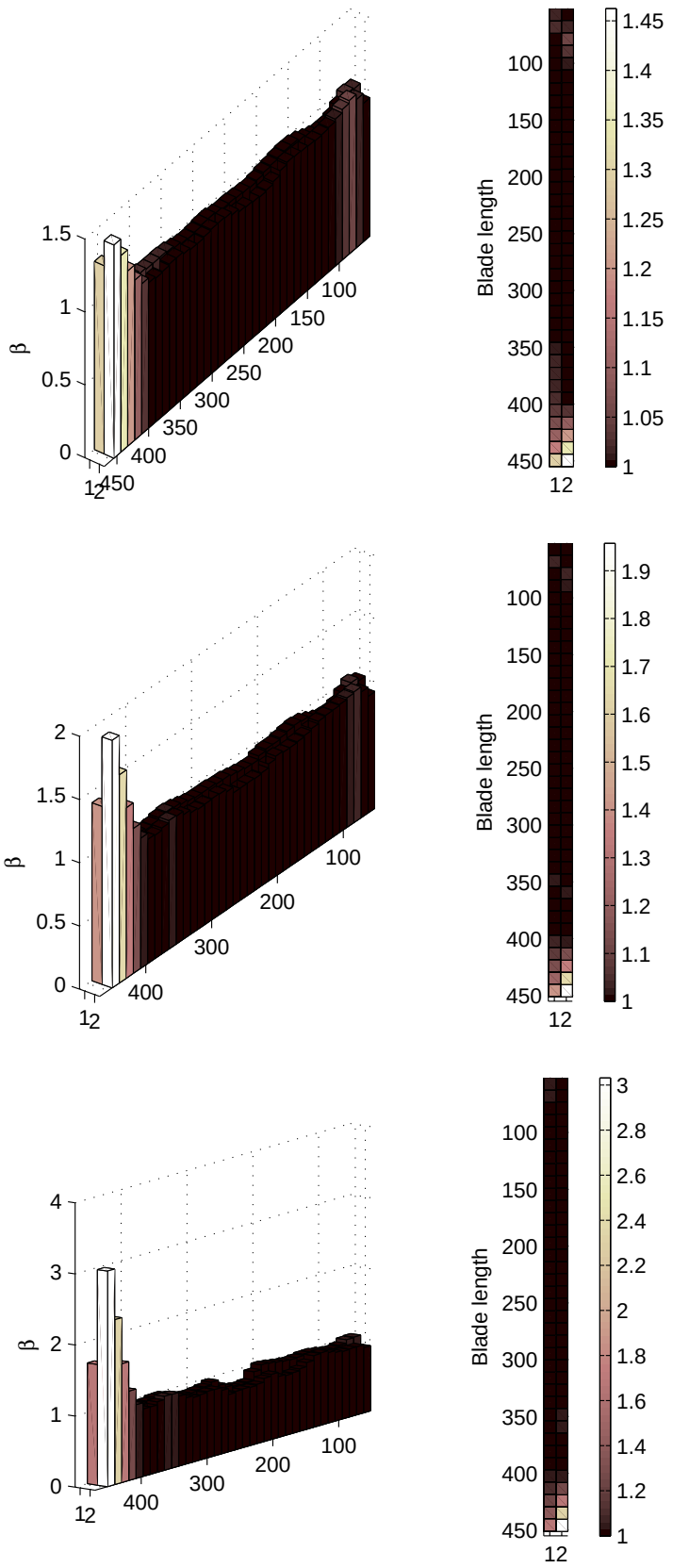

Figure C.1: MSEDI, Case 1.1 L,M and H in 3D and top view.

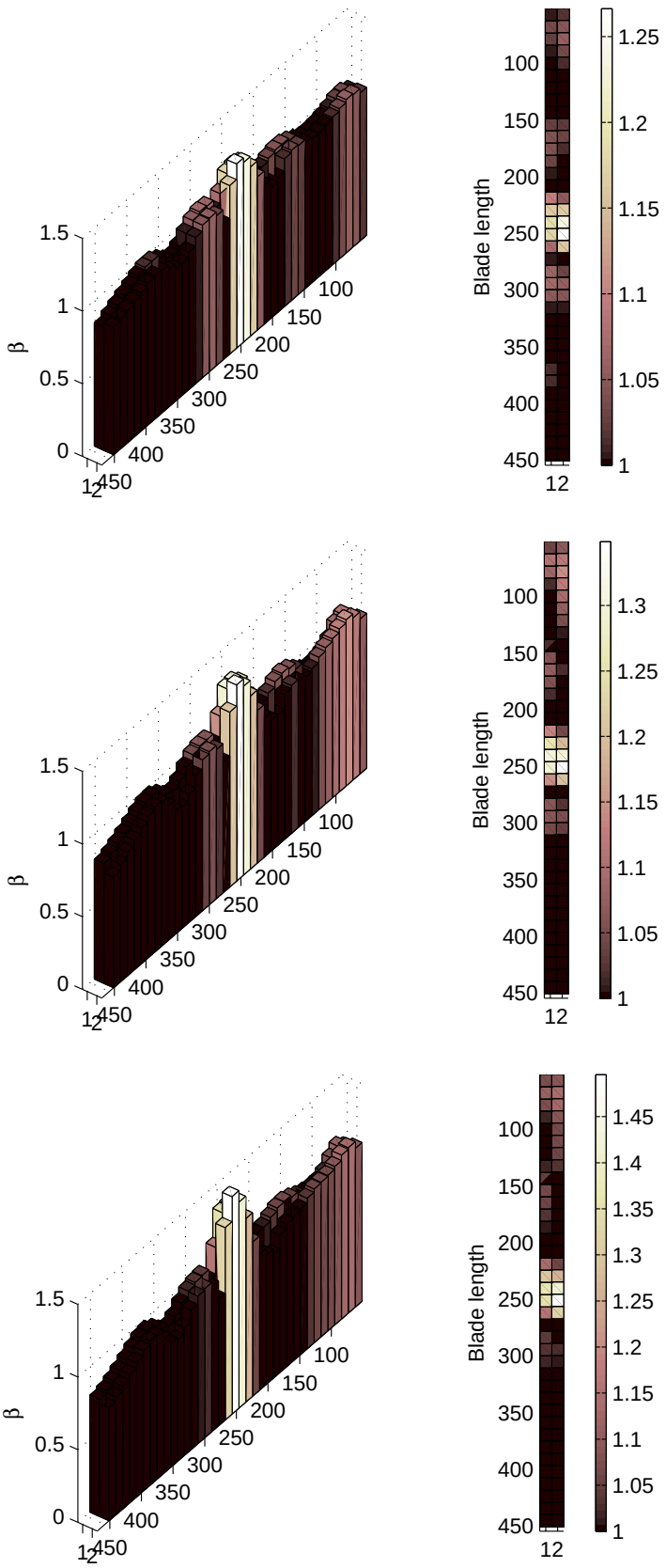

Figure C.2: MSEDI, Case 1.2 L,M and H in 3D and top view.

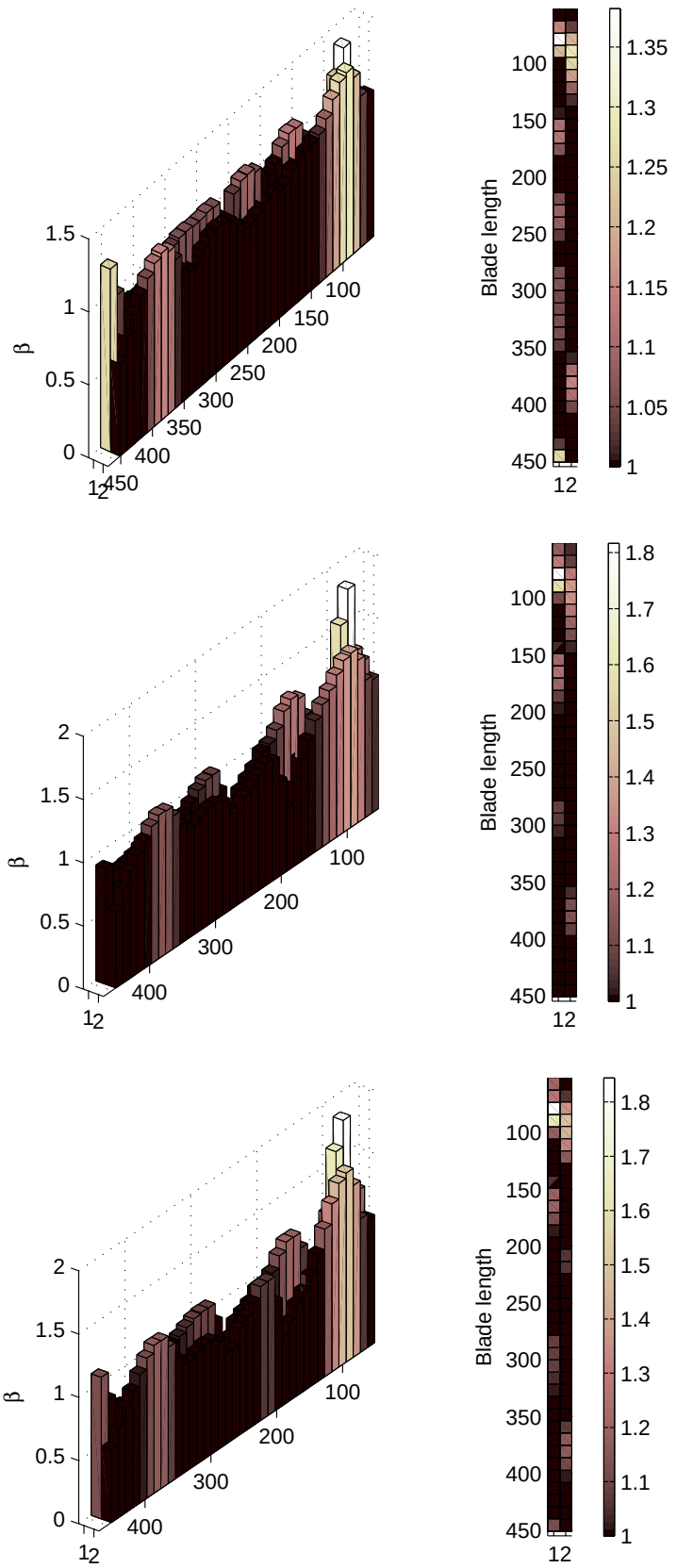

Figure C.3: MSEDI, Case 1.3 L,M and H in 3D and top view.

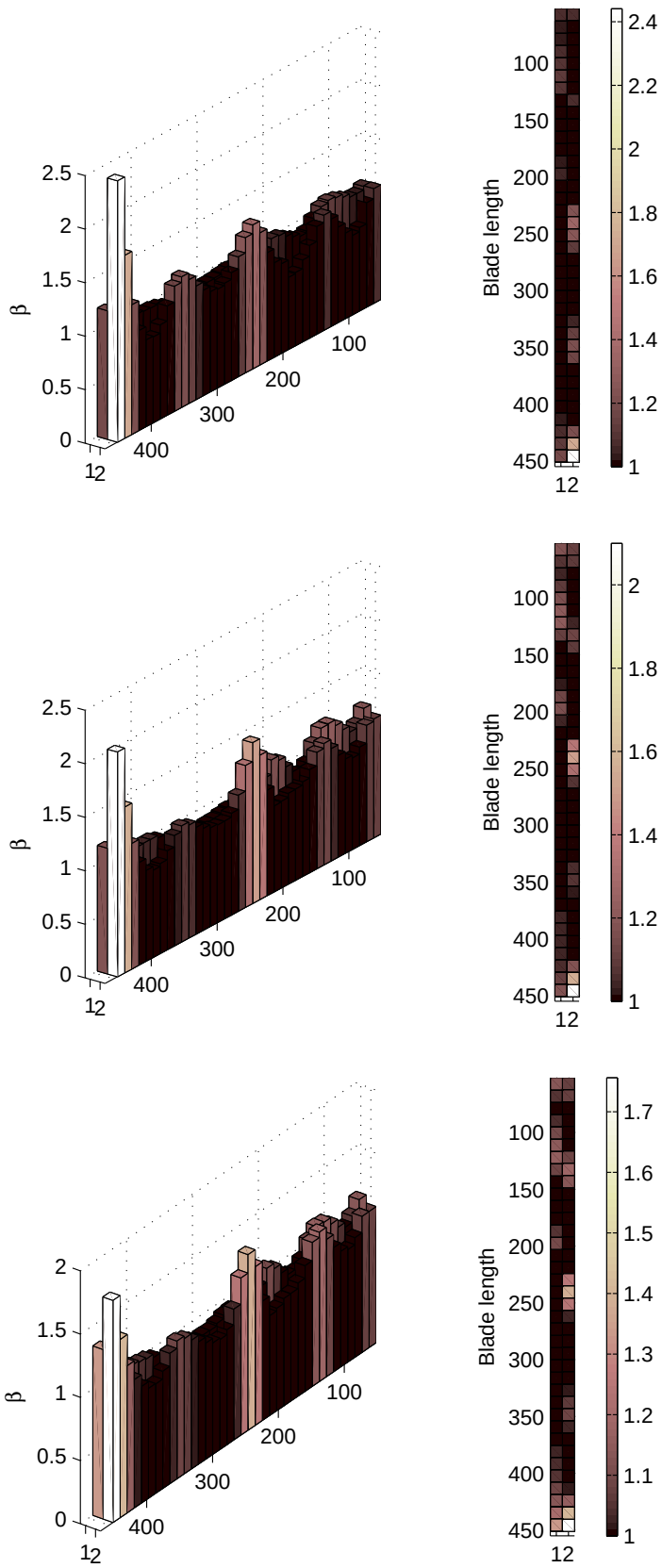

Figure C.4: MSEDI, Case 1.4 L,M and H in 3D and top view.

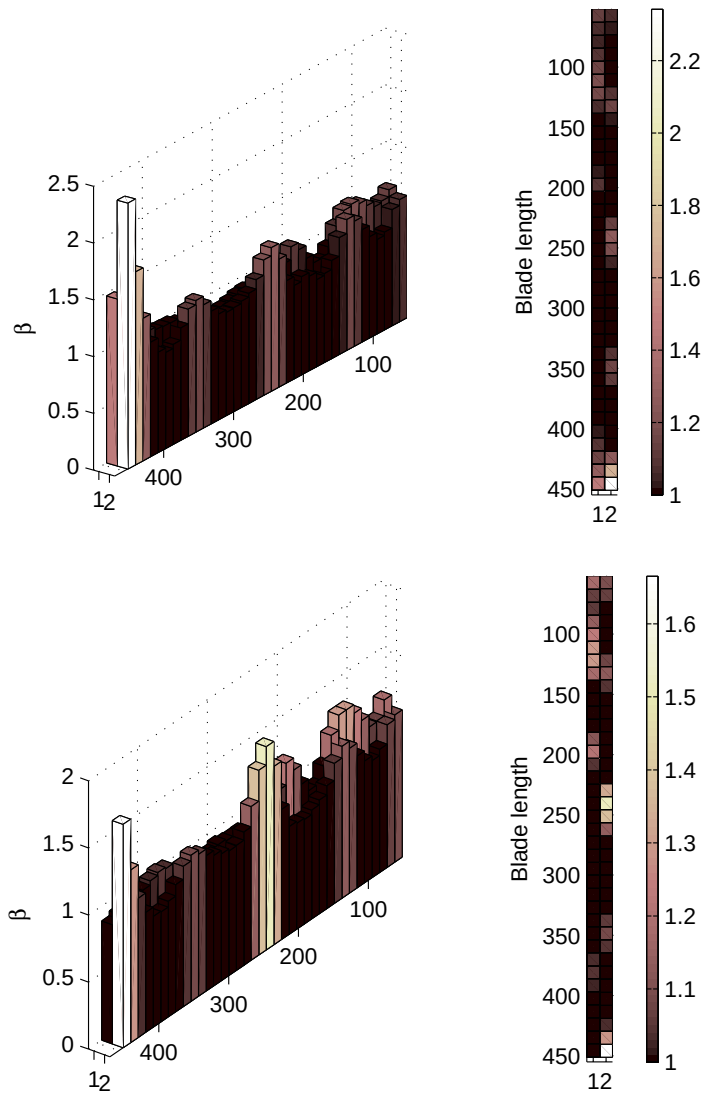

Figure C.5: MSEDI, Case 1.5 HL and LH in 3D and top view.

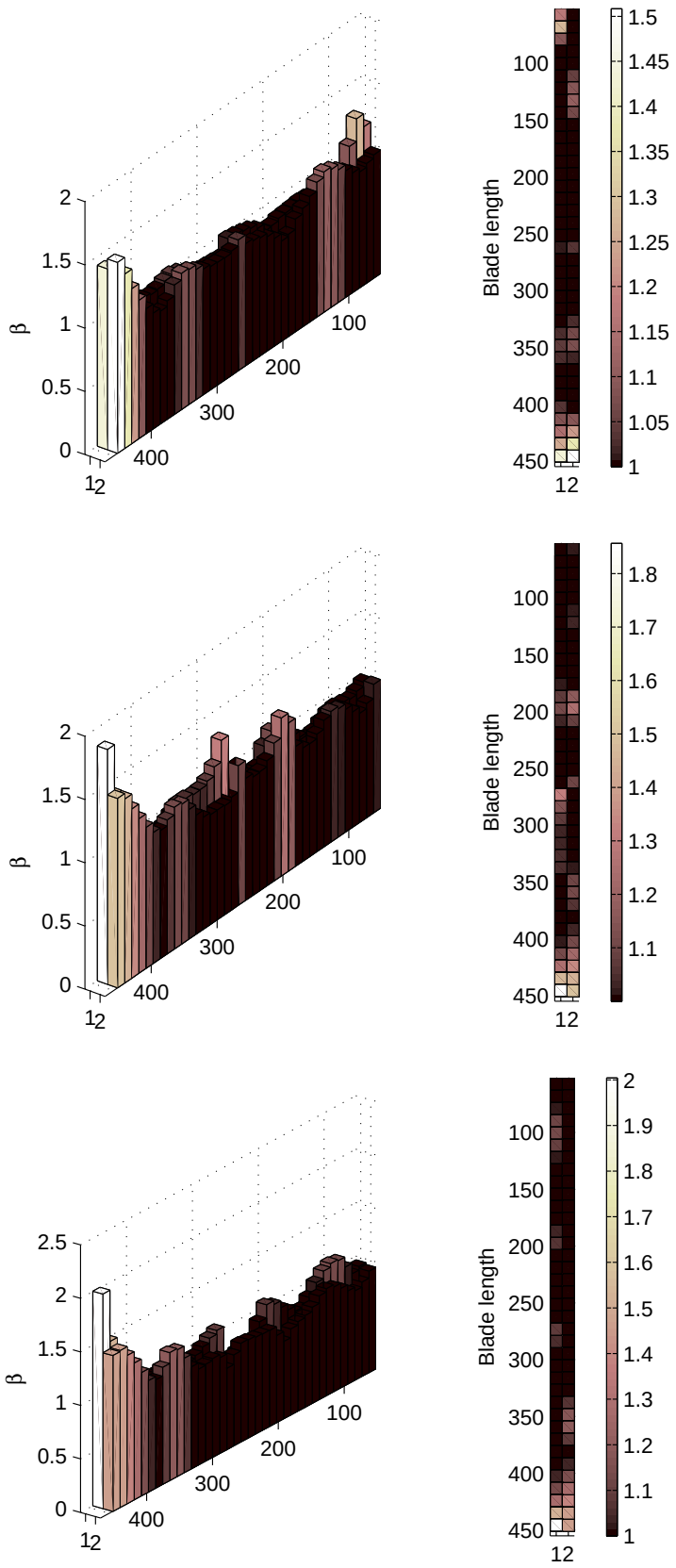

Figure C.6: MSEDI, Case 2.1 L,M and H in 3D and top view.

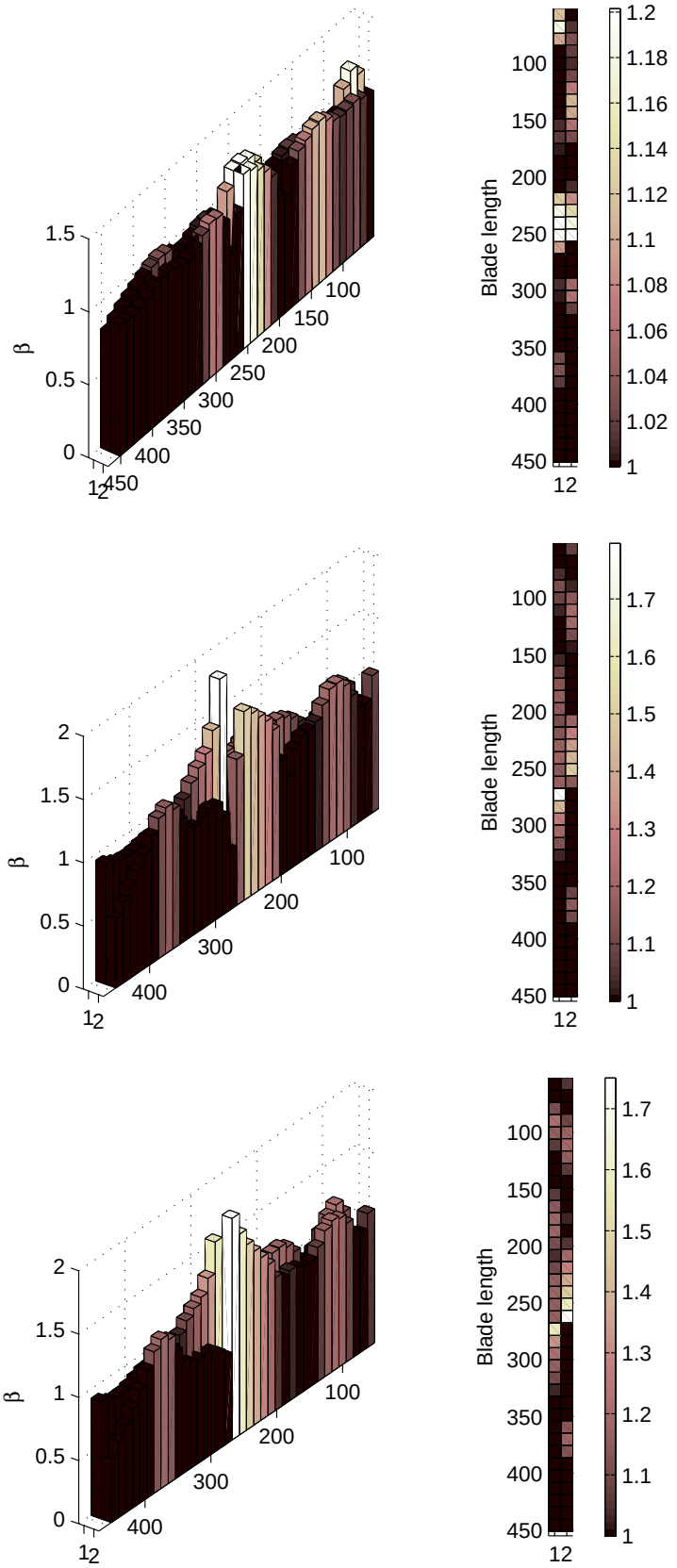

Figure C.7: MSEDI, Case 2.2 L,M and H in 3D and top view.

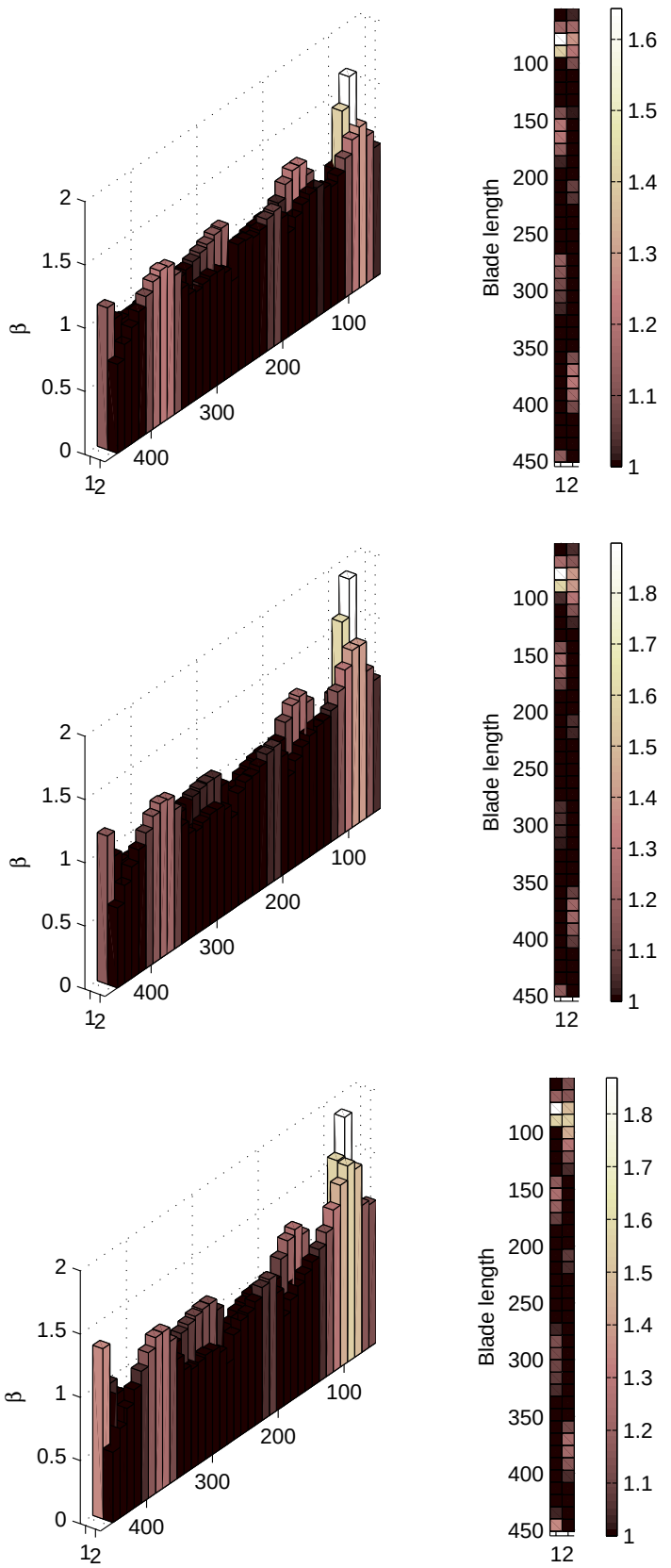

Figure C.8: MSEDI, Case 2.3 L,M and H in 3D and top view.

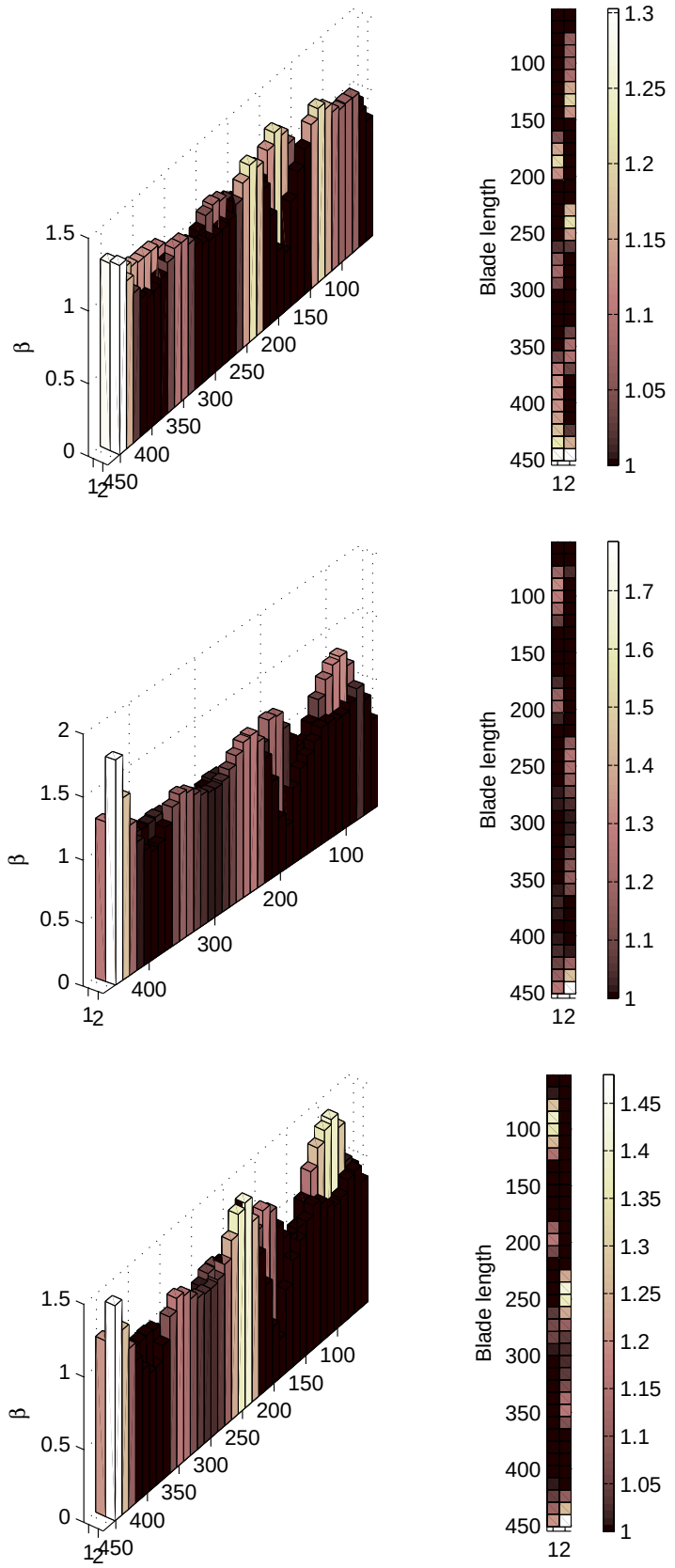

Figure C.9: MSEDI, Case 2.4 L,M and H in 3D and top view.

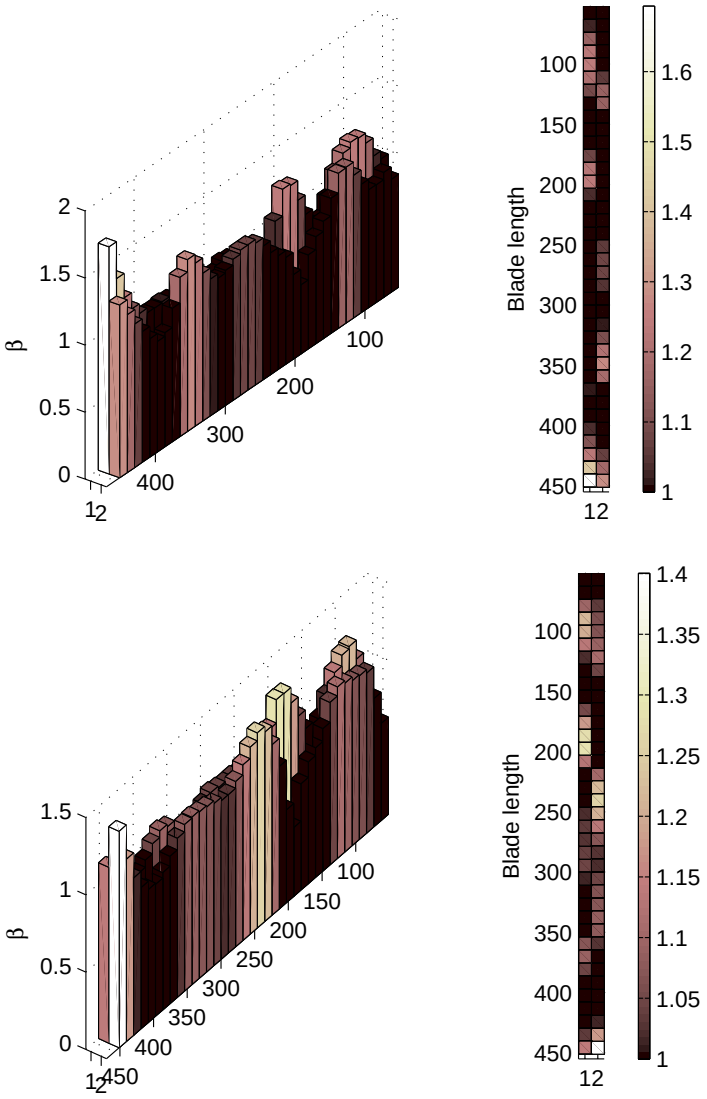

Figure C.10: MSEDI, Case 2.5 HL and LH in 3D and top view.